UNC-45a promotes myosin folding and stress fiber assembly

Jaakko I. Lehtimäki,[1] Aidan M. Fenix,[4] Tommi M. Kotila,[1] Giuseppe Balistreri,[2] Lassi Paavolainen,[3] Markku Varjosalo,[1] Dylan T. Burnette,[4] and Pekka Lappalainen[1]

[1]Institute of Biotechnology, [2]Department of Biosciences, Division of General Microbiology, and [3]Institute for Molecular Medicine Finland (FIMM), University of Helsinki, Helsinki, Finland
[4]Department of Cell and Developmental Biology, Vanderbilt University School of Medicine, Nashville, TN

Contractile actomyosin bundles, stress fibers, are crucial for adhesion, morphogenesis, and mechanosensing in nonmuscle cells. However, the mechanisms by which nonmuscle myosin II (NM-II) is recruited to those structures and assembled into functional bipolar filaments have remained elusive. We report that UNC-45a is a dynamic component of actin stress fibers and functions as a myosin chaperone in vivo. UNC-45a knockout cells display severe defects in stress fiber assembly and consequent abnormalities in cell morphogenesis, polarity, and migration. Experiments combining structured-illumination microscopy, gradient centrifugation, and proteasome inhibition approaches revealed that a large fraction of NM-II and myosin-1c molecules fail to fold in the absence of UNC-45a. The remaining properly folded NM-II molecules display defects in forming functional bipolar filaments. The C-terminal UNC-45/Cro1/She4p domain of UNC-45a is critical for NM-II folding, whereas the N-terminal tetratricopeptide repeat domain contributes to the assembly of functional stress fibers. Thus, UNC-45a promotes generation of contractile actomyosin bundles through synchronized NM-II folding and filament-assembly activities.

Introduction

Polymerization of actin filaments against cellular membranes generates force for cell migration, morphogenesis, and endocytosis (Blanchoin et al., 2014). These branched actin networks and bundles also serve as tracks for cargo transport by unconventional myosins (Mehta et al., 1999; Wells et al., 1999; Berg and Cheney, 2002). Moreover, actin filaments, together with type II myosins, form contractile structures, such as muscle myofibrils and stress fibers of nonmuscle cells. In skeletal muscle cells, the bipolar myosin II filaments form regular structures with bipolar arrays of actin filaments to provide force for muscle contraction. Similarly, the stress fibers, which have an important role in cell adhesion, morphogenesis, and mechanosensing, as well as in protecting the nucleus during confined migration, are composed of bipolar arrays of actin and nonmuscle myosin II (NM-II) filaments (Tojkander et al., 2012; Skau et al., 2016).

The NM-II molecule is composed of two essential light chains and two regulatory light chains that bind to two heavy chains. The N-terminal region of the heavy chain harbors the motor domain, which possesses both ATPase activity and actin-binding interfaces. The N-terminal region is followed by a neck domain that transits actin translocation forces in a lever

fashion (Vicente-Manzanares et al., 2009). The C-terminal tails of heavy chains are responsible for entwining NM-II molecules into bipolar filaments that are able to slide actin filaments with different polarities toward the center of the myosin filament (Niederman and Pollard, 1975; Billington et al., 2013; Fenix et al., 2016). In muscles, continuous tensile forces are known to disrupt and damage the myosin II–containing contractile units (McNeil and Khakee, 1992; Clarke et al., 1995; Gibala et al., 1995; Etard et al., 2008; Paulsen et al., 2009; Melkani et al., 2011). The turnover of myosin II in contractile actomyosin arrays must also be balanced by incorporation of new myosin II molecules into those structures (Vicente-Manzanares et al., 2007; Sandquist and Means, 2008). These features, together with the complex folding of the motor domain through multiple transitional states (Chow et al., 2002), call for the presence of chaperones. Folding of both invertebrate and vertebrate muscle myosin II molecules are catalyzed by ubiquitous heat-shock proteins 90 (Hsp90) and 70 (Hsp70) assisted by UNC-45, which belongs to the conserved UNC-45/Cro1/She4p (UCS) family of myosin chaperones (Barral et al., 2002; Lee et al., 2014).

UNC-45 was initially discovered as a temperature-sensitive mutation in *Caenorhabditis elegans*, causing partial

Supplemental material can be found at:
http://doi.org/10.1083/jcb.201703107

paralysis and disorganized myofibrils (Epstein and Thomson, 1974). Subsequently, the UNC-45 protein was shown to be important for the correct functioning and organization of myosin II in invertebrate muscle myofilaments (Barral et al., 1998; Venolia et al., 1999; Lee et al., 2011). UNC-45 consists of an N-terminal tetratricopeptide repeat (TPR) domain enabling interaction with Hsp90 and Hsp70 (Barral et al., 2002), a central domain, and a subsequent neck domain, followed by a conserved C-terminal UCS domain that interacts with the myosin II motor domain (Barral et al., 2002; Price et al., 2002; Gazda et al., 2013). Structural work on *C. elegans* UNC-45 (ceUNC-45) provided evidence for a scaffolding model, in which the TPR domain binds the neck domain of an adjacent UNC-45 molecule to generate short, linear chains, with spacing of the individual UNC-45–Hsp90 complexes coinciding with myosin II spacing in nematode myofilaments (Gazda et al., 2013). Mutational studies suggested that UNC-45 contributes to both myosin II folding (through its UCS domain) and to proper assembly of myosin II filaments (through TPR and neck domains) in *C. elegans* muscles, although the relative importance of those activities have not been tested in cells directly (Ni et al., 2011; Gazda et al., 2013).

Although invertebrates express a single UNC-45 protein, vertebrates have two UNC-45 isoforms: muscle-specific UNC-45b and a nonmuscle isoform UNC-45a (Price et al., 2002; Anderson et al., 2008). However, only the function of UNC-45b has been linked to myosin II–dependent processes in cells. UNC-45b colocalizes with myosin II in myofibrils and is required for their proper assembly in *Xenopus* species, zebrafish, and mouse cardiac and/or skeletal muscles (Wohlgemuth et al., 2007; Etard et al., 2008; Srikakulam et al., 2008; Geach and Zimmerman, 2010; Chen et al., 2012). Although UNC-45a can enhance folding of smooth muscle myosin II in vitro in the presence of Hsp90 (Liu et al., 2008), it has not been linked to either NM-II folding in cells or in the assembly of contractile actomyosin bundles. In the nonmuscle cells studied so far, UNC-45a displays relatively uniform cytoplasmic localization, apart from accumulation to immunologic synapses in natural killer cells and to the cleavage furrow of ovarian cancer cells (Chadli et al., 2006; Bazzaro et al., 2007; Iizuka et al., 2015). Antisense, RNAi, and overexpression studies have provided evidence that UNC-45a contributes to the proliferation and invasiveness of ovarian and breast cancer cells and to exocytosis of lytic granules in natural killer cells (Price et al., 2002; Bazzaro et al., 2007; Guo et al., 2011). However, apart from slightly reduced NM-II binding to actin filaments, the UNC-45a knockdown cells did not display detectable defects in either NM-II folding or the assembly of actomyosin bundles (Chadli et al., 2006; Bazzaro et al., 2007; Guo et al., 2011; Iizuka et al., 2015). Interestingly, UNC-45a has also been linked to other functions, including progesterone receptor folding and retinoic acid signaling (Chadli et al., 2006; Epping et al., 2009). Thus, whether UNC-45a contributes to the assembly of NM-II filaments in nonmuscle cells or functions as a general chaperone for other proteins has not been determined to date. In addition, muscle and NM-II filaments display some key structural differences (Craig and Woodhead, 2006; Billington et al., 2013; Thoresen et al., 2013; Shutova et al., 2014; Fenix et al., 2016), which may result in muscle and NM-II isoforms having distinct requirements for chaperones and filament-assembly factors.

Results

UNC-45a displays dynamic localization to contractile stress fibers

Previous studies suggested that UNC-45a displays largely diffuse cytoplasmic localization in nonmuscle cells, and specific accumulation of UNC-45a to actomyosin bundles has not been reported (Chadli et al., 2006; Bazzaro et al., 2007; Iizuka et al., 2015). Stress fibers are the most pronounced myosin II–containing actin-filament bundles in most nonmuscle cells. We used human U2OS osteosarcoma cells, which have been extensively applied as a model system to study stress fiber assembly, mechanosensitivity, and turnover (Hotulainen and Lappalainen, 2006; Burnette et al., 2014; Schulze et al., 2014; Tojkander et al., 2015), to examine whether UNC-45a associates with those contractile actomyosin bundles.

Immunofluorescence (IF) microscopy with an antibody that recognized the full-length protein revealed that UNC-45a localized to the lamella in U2OS cells and was enriched in NM-II–containing actin stress fibers (Fig. 1 A). There was, however, significant cell-to-cell variation in UNC-45a protein levels and subcellular localizations, and clear UNC-45a accumulation to stress fibers was distinguishable in ~30% of the cells (Fig. S1 A). To confirm the stress fiber localization of UNC-45a, we also used GFP-fusion proteins. In cells overexpressing UNC-45a–GFP, the protein displayed primarily diffuse cytoplasmic localization. However, when the "unbound" pool of proteins was extracted, UNC-45a–GFP localized to NM-II–containing stress fibers (Fig. S2 A). The stress fiber localization of UNC-45a appears to be mediated by the myosin II–binding UCS domain because UNC-45a mutants that lack the N-terminal TPR domain (ΔTPR) and the isolated UCS domain localized to stress fibers (Fig. S2 A).

We next examined the dynamics of UNC-45a stress fiber association with photoactivatable GFP (paGFP) fusion constructs that enabled us to circumvent the signal from the cytoplasmic UNC-45a pool, which prevents reliable measurements of fluorescence recovery after photobleaching. We photoactivated distinct regions of stress fibers, which were made visible by cotransfecting the cells with an mApple–NM-IIA construct (Figs. 1 B and S1, B and C). NM-IIA–paGFP displayed relatively slow dynamics in stress fibers, consistent with previously reported fluorescence recovery after photobleaching experiments (Vicente-Manzanares et al., 2007; Sandquist and Means, 2008). Whether NM-IIA dynamics occurs through the exchange of individual subunits within the filament or through depolymerization of the entire filament and shares similarities with the cortical NM-IIA pulses (Baird et al., 2017) remains to be elucidated. Importantly, UNC-45a–paGFP displayed ~10-fold more-rapid dynamics that was, nevertheless, slower than "cytoplasmic" UNC-45a, which was not associated with NM-IIA–positive stress fibers (Figs. 1 C and S1, B and C). Interestingly, although the dynamics of UNC-45a-paGFP was rapid on stress fibers, it exhibited much slower fluorescence dissipation in the mApple-NM-IIA–positive aggregates that were occasionally observed in transfected U2OS cells (Fig. S1 C, yellow arrow).

Together, those data demonstrate that UNC-45a localizes to the NM-II–containing actin stress fibers and that this localization appears to be mediated by the C-terminal UCS domain of the protein. Photoactivation experiments provided evidence that UNC-45a exhibits rapid association/dissociation kinetics
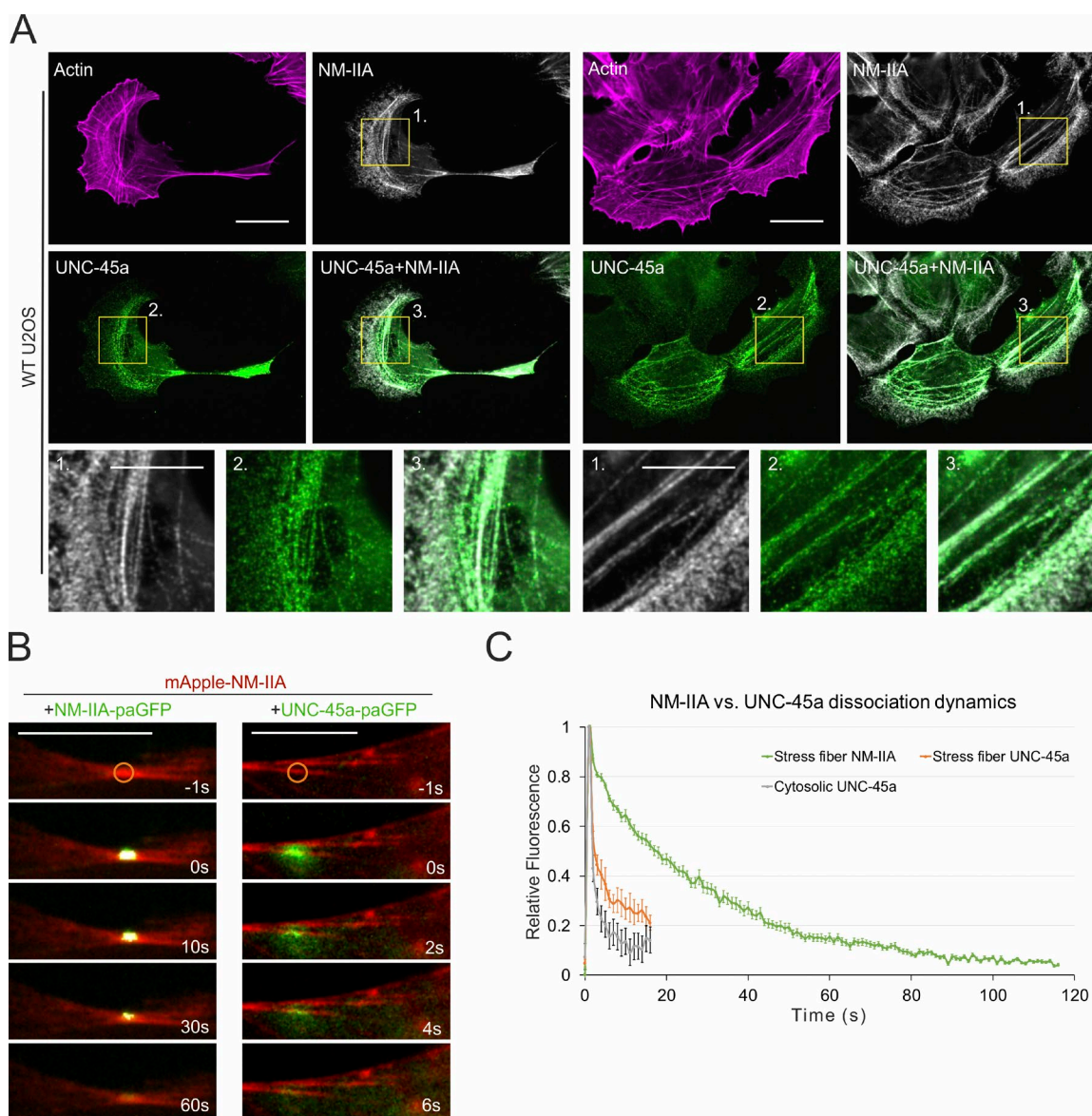
Figure 1. **UNC-45a localizes to contractile stress fibers with rapid association–dissociation dynamics.** (A) IF of endogenous actin, NM-IIA, and UNC-45a in U2OS cells detected by phalloidin, polyclonal NM-IIA heavy chain and polyclonal UNC-45a antibodies, respectively. Magnified regions (indicated by numbers) illustrate the colocalization of NM-IIA and UNC-45a. Bars: (main) 20 µm; (insets) 10 µm. (B) Time-lapse images of photoactivation experiments revealing the dynamics of photoactivatable–GFP fusion constructs (paGFP) of NM-IIA and UNC-45a in stress fibers. U2OS cells were cotransfected with mApple–NM-IIA together with either NM-IIA–paGFP or UNC-45a–paGFP. The fluorescence of paGFP fusion proteins at discrete spots (indicated by orange circles) of mApple–NM-IIA–positive stress fibers were activated with a 405-nm laser pulse, and the dispersion of the photoactivated fluorophore was followed. Bar, 15 µm. (C) Quantification of the dynamics of stress fiber associated NM-IIA (green line), UNC-45a (orange line), and cytosolic UNC-45a (gray line). The rates of the photoactivated fusion protein dissociation from stress fibers, and UNC-45a dissipation from cytosolic regions devoid of stress fibers were measured by following the paGFP signal dispersion on activated foci (exemplified with orange squares in B) and normalized to the background (cytoplasmic) signal at each time point. Data acquisition was continued until fluorescence reached the preactivation level. The data are presented as means ± SEM. For cytosolic and stress fiber–bound UNC-45a, n = 5 photoactivated foci from two UNC-45a–paGFP transfected cells and n = 7 photoactivated foci from two NM-IIA–paGFP transfected U2OS cells.

on stress fibers but displays more-stable binding to myosin II–containing aggregates.

UNC-45a is critical for stress fiber assembly and tail retraction during cell migration

RNAi and antisense oligonucleotide-based depletions of UNC-45a resulted in relatively mild phenotypes without significant effects on NM-II protein levels, myosin regulatory light chain (RLC) phosphorylation, or the morphology of contractile acto-

myosin bundles (Price et al., 2002; Bazzaro et al., 2007; Comyn and Pilgrim, 2012; Iizuka et al., 2015). Similarly, depletion of UNC-45a from U2OS cells by RNAi did not result in dramatic effects on cell morphology or on the actin cytoskeleton, although the knockdown cells displayed mild defects in the assembly of ventral stress fibers (Fig. S3, B and C). However, because of the significant variation in UNC-45a protein levels between individual U2OS cells and because siRNA treatment did not result in a complete loss of the UNC-45a protein, we generated UNC-45a knockout cells by the CRISPR/Cas9
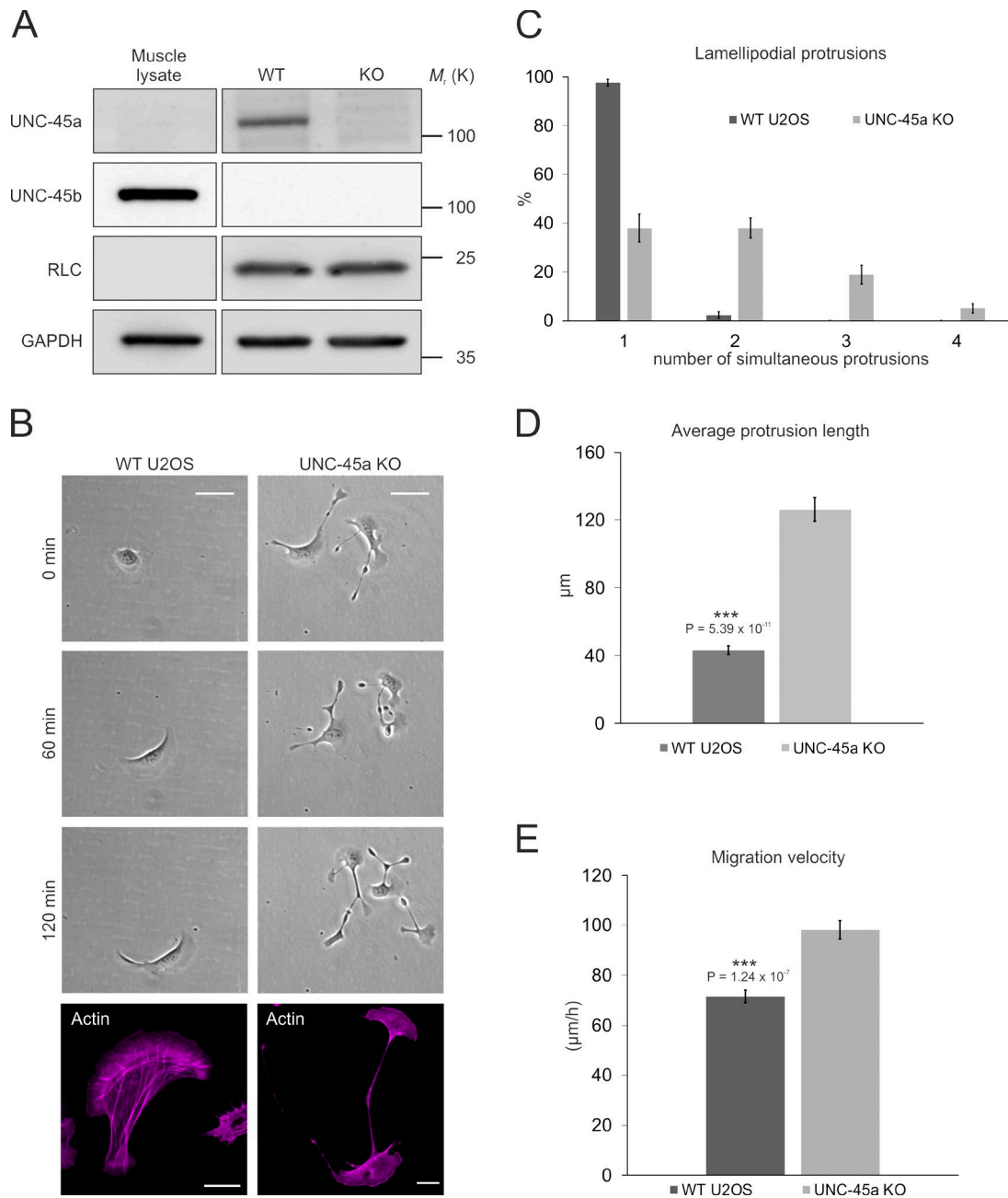
Figure 2. **UNC-45a knockout cells display abnormal cell morphology accompanied by multiple lamellipodial protrusions and deficient tail retraction.** (A) WB analysis of endogenous UNC-45a, UNC-45b, and myosin RLC levels in total cell lysates of WT U2OS and UNC-45a knockout (KO) U2OS cells. Human skeletal muscle lysate was used as a positive control for UNC-45b expression, and GAPDH was probed for equal sample loading. (B) Time-lapse images of WT and UNC-45a knockout cells migrating on a laminin-coated surface, and representative examples of endogenous F-actin localization (by fluorescent phalloidin) in WT and UNC45a knockout cells cultured on laminin-coated coverslips. Bars, 50 µm (time-lapse images) and 20 µm (fixed cells stained with fluorescent phalloidin). (C) Lamellipodial-protrusion profiles of randomly migrating WT and UNC-45a knockout cells were tracked for 80 min. The number of lamellipodial protrusions was quantified every 10 min, and the data are presented as the percentage of cells exhibiting one, two, three, or four simultaneous protrusions; means ± SEM, n = 27 WT and 27 UNC-45a knockout cells. (D) Protrusion lengths (vector distance from the edge of nucleus to the furthest cell edge) of randomly migrating WT and UNC-45a knockout cells. The data are presented as protrusion length means ± SEM. n = 20 WT and 20 UNC-45a knockout cells. (E) Random migration velocities of WT and UNC-45a knockout cells. Quantification is based on tracking of the nuclei displacement. The data are presented as velocity obtained from a 10-h cell tracking; means ± SEM. n = 40 for WT and 34 for UNC-45a knockout cells. (C–E) Quantifications were performed from the time-lapse phase-contrast imaging data, exemplified in B, and a Student's t test was used to derive the p-values. Fig. S5 E provides data for a cell-migration rescue experiment for UNC-45a knockout cells.

approach. Those cells completely lacked the UNC-45a protein, with no detected, compensatory up-regulation of the UNC-45b isoform (Figs. 2 A and S2 C).

Importantly, the UNC-45a knockout cells displayed a drastic migratory phenotype, defined by deficient tail retraction

and multiple lamellipodial protrusions extending in different directions (Fig. 2, B–D; and Videos 1 and 2). Despite the splayed migratory phenotype, UNC-45a knockout cells manifested faster random-migration velocity in the 2D environment compared with control cells (Fig. 2 E), which is similar
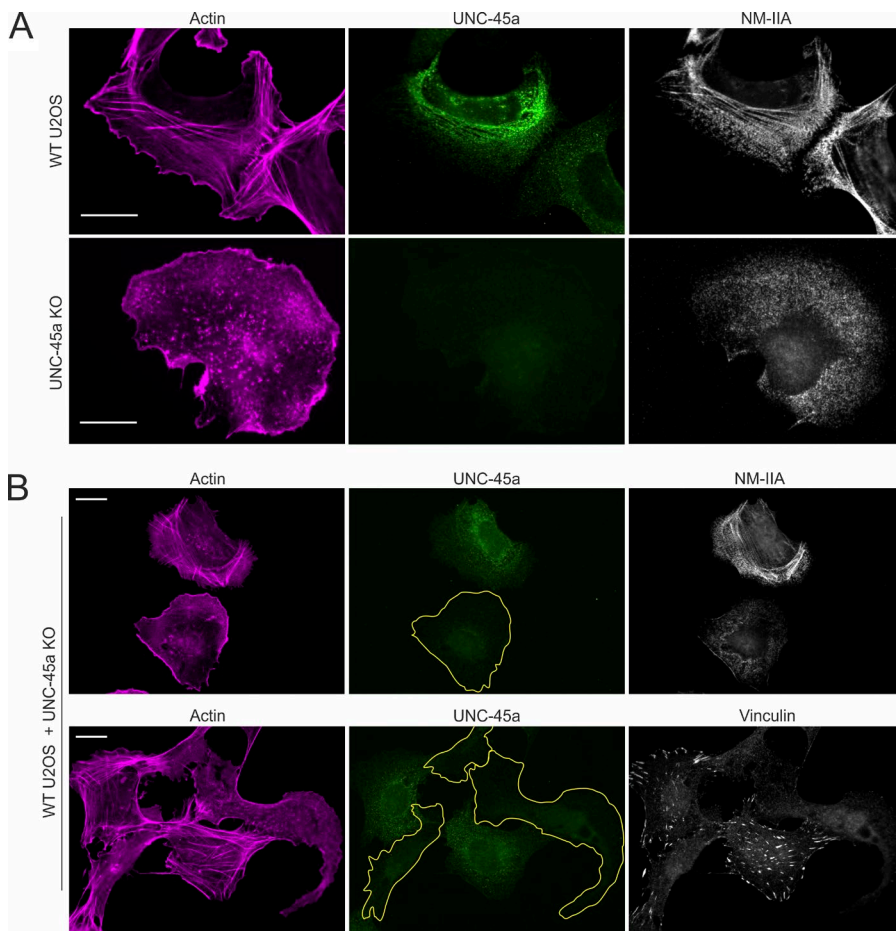
Figure 3. **UNC-45a depletion impairs stress fiber assembly and focal adhesion maturation.** (A) Visualization of actin filaments, endogenous UNC-45a, and NM-IIA heavy chains in WT and UNC-45a knockout (KO) cells (cultured on noncoated coverslips). (B) Co-cultivated WT and UNC-45a knockout cells stained for F-actin (phalloidin), UNC-45a, NM-IIA heavy chains, and vinculin. Yellow outlines indicate the borders of UNC-45a knockout cells. Bars, 20 µm.

to the previously reported effects of NM-IIA depletion on cell migration (Shih and Yamada, 2010; Jorrisch et al., 2013). IF microscopy revealed that stress fibers are largely absent from UNC-45a knockout cells and that NM-II displays uniform punctate, cytoplasmic localization (Figs. 3 A and S3 A). The remaining stress fibers in the knockout cells were typically very faint and did not assemble into thick, contractile bundles. Consistent with an increased migration velocity and the absence of contractile stress fibers, vinculin-positive focal adhesions were also diminished in UNC-45a knockout cells (Fig. 3 B, bottom). Collectively, these knockout experiments revealed that UNC-45a is critical for stress fiber assembly, and hence, its absence leads to defects in cell adhesion, migration, and tail retraction.

UNC-45a is important for myosin II and myosin 1c folding in vivo

UNC-45a deletion not only resulted in a loss of stress fibers and accompanying uniform localization pattern of NM-II but also led to diminished NM-II protein levels, which was most obvious in experiments in which control and UNC-45a knockout cells were co-cultivated together and stained with myosin antibodies. Intensities of both NM-IIA and NM-IIB were much fainter in knockout cells compared with control cells (Figs. 3 B, top; and Fig. S3 A). Furthermore, Western blot (WB) analysis revealed a mean of 60% and 70% decrease in NM-IIA and NM-IIB protein levels, respectively, in UNC-45a knockout cells compared with WT U2OS cells (Figs. 4 A and S2 B). The decrease in NM-II occurred at the protein level because the expression levels of *MYH9* (which encodes NM-IIA) and *MYH10* (which encodes

NM-IIB) mRNAs were unaffected by UNC-45a depletion (Fig. 4 B). Moreover, phosphorylation of RLC (as detected by an antibody recognizing T18/S19 di-phosphorylated proteins) that is required for NM-II filament formation and increases actin-activated ATPase activity (Umemoto et al., 1989; Burgess et al., 2007) was twofold elevated in UNC-45a knockout cells (Figs. 4 A and S2 C). That increase may result from increased accessibility to the phosphorylation sites in RLC when it is not bound to a myosin heavy chain or be due to a compensation for the diminished NM-II levels with increased myosin activation. In contrast, depletion of UNC-45a had no effect on the protein levels of its reported binding partner Hsp90β (Chadli et al., 2008) or on the levels of β-actin (Fig. S2 B).

UNC-45 from *Drosophila* species protects the skeletal muscle myosin II from heat-induced aggregation, and myosin aggregates have been documented in UNC-45 RNAi-treated *C. elegans* (Melkani et al., 2010; Gaiser et al., 2011). However, besides the decline in NM-II levels, no apparent myosin II aggregates were observed in UNC-45a knockout cells. To examine whether the diminished NM-II levels in UNC-45a knockout cells resulted from myosin folding problems, we applied the MG-132 compound, which reversibly inhibits 26S proteasome, which was previously reported to degrade myosin in *C. elegans* (Lee and Goldberg, 1998; Henderson et al., 2005; Landsverk et al., 2007). Although acute proteasome inhibition in WT U2OS cells with 10 µM MG-132 did not result in visible changes in the actomyosin cytoskeleton, identical treatment of UNC-45a knockout cells led to an appearance of numerous NM-IIA– and NM-IIB–positive aggregates in the cytoplasm (Fig. 4 C and
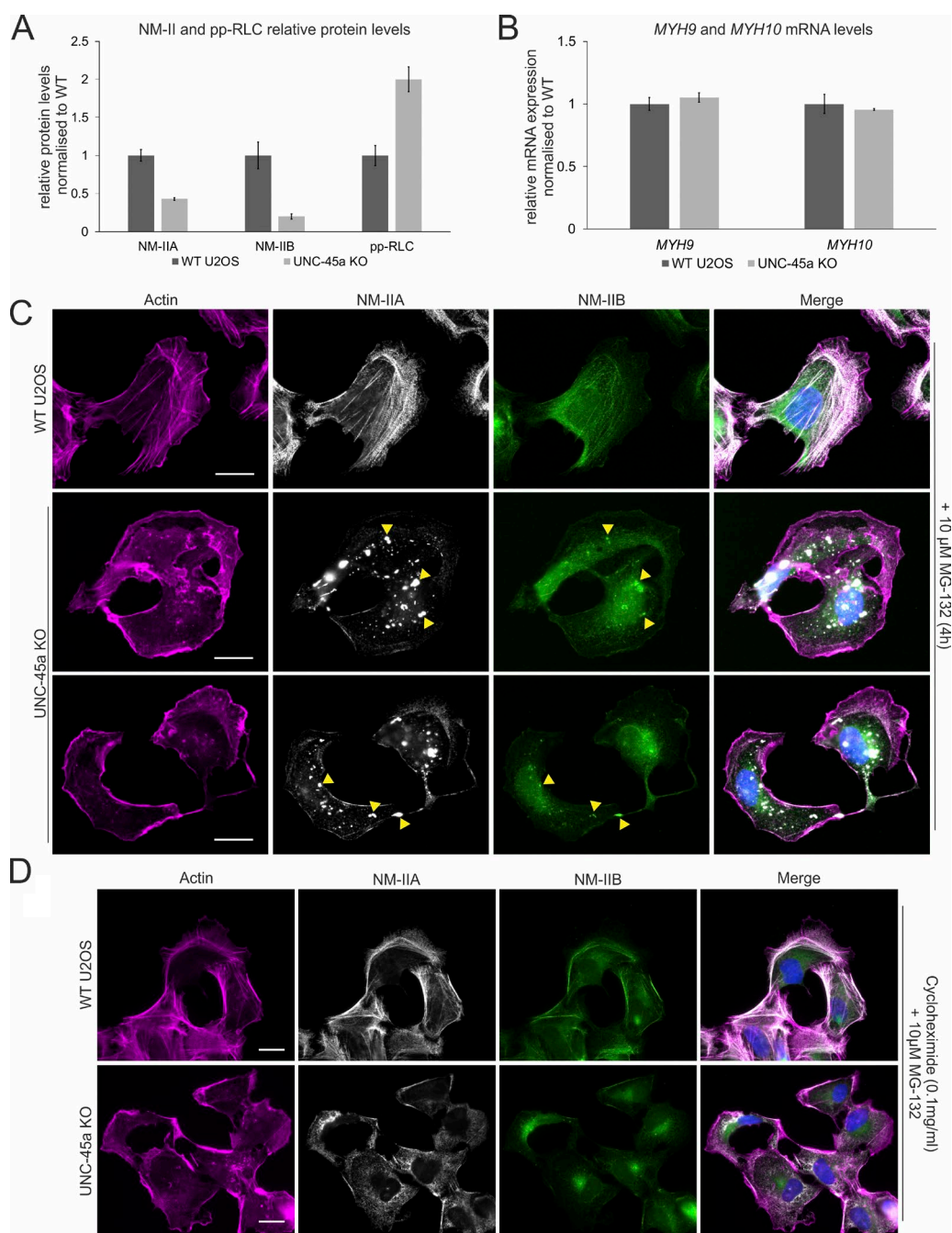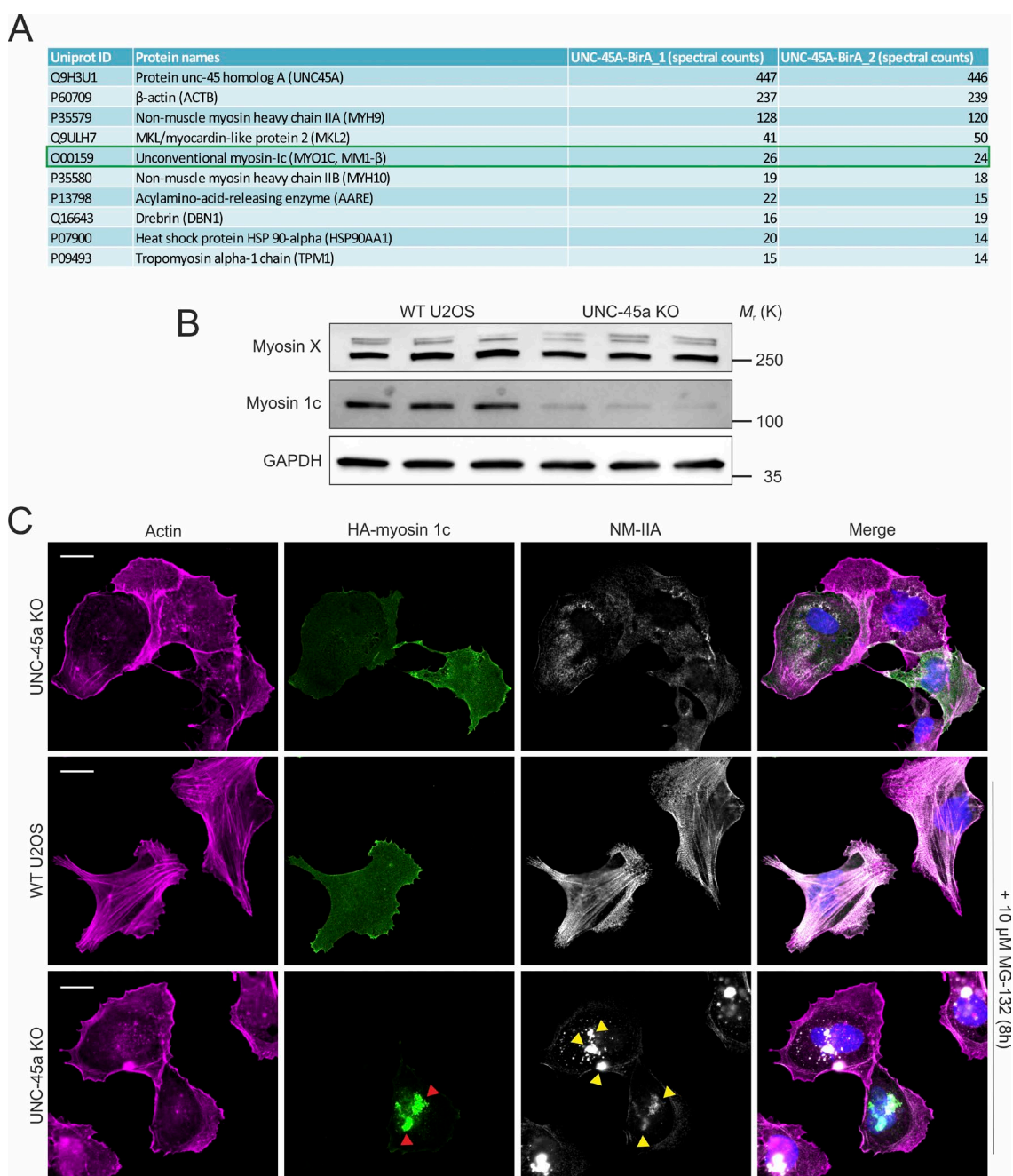
Figure 4. **UNC-45a depletion predisposes nascent NM-II for aggregation.** (A) Relative protein levels of NM-IIA, NM-IIB, and pp(T18, S19)–RLC were analyzed by WB from WT and UNC-45a knockout (KO) cell lysates. The NM-IIA/B and pp-RLC levels in WT cells were set to 1, and the data are presented as means ± SEM, $n = 3$ WT and 3 UNC-45a knockout total cell lysates. (B) Quantification of *MYH9* (NM-IIA) and *MYH10* (NM-IIB) mRNA levels in WT and UNC-45a knockout cells. GAPDH was used as the control to derive the ΔCt values. The data are presented as $2^{-\Delta\Delta Ct}$ ± SEM, $n = 4$ (mRNAs extracted from 4 WT and 4 UNC-45a knockout cultures, converted to cDNAs, and analyzed by quantitative PCR). (C) WT and UNC-45a knockout cells were treated for 4 h with 10 µM MG-132 proteasome inhibitor. Yellow arrowheads indicate examples of NM-IIA and NM-IIB containing aggregates in UNC-45a knockout cells. Bars, 20 µm. Fig. S4 A shows a similar analysis of other UNC-45a knockout cell clones obtained. (D) Treatment of WT and UNC-45a knockout cells with a combination of the protein synthesis inhibitor cycloheximide (0.1 mg/ml) and MG-132 (10 µM) for 4 h. Bars, 20 µm. (C and D) F-actin was visualized with phalloidin. NM-IIA and NM-IIB heavy chains and nuclei were detected with polyclonal antibodies and DAPI, respectively.

Fig. S4, A and B). When the knockout cells were simultaneously treated with MG-132 and the protein-synthesis inhibitor cycloheximide, the appearance of myosin II aggregates was inhibited, suggesting that their formation results primarily from defects in the folding of nascent myosin II heavy chains (Fig. 4 D).

We also performed proximity-dependent biotin ligation (BioID) experiments (Roux et al., 2012) to identify binding partners for UNC-45a. That approach revealed that, in addition to NM-IIA and NM-IIB, an unconventional myosin 1c was among the most-abundant UNC-45a interactors in U2OS cells. Those three proteins were also the only myosin family proteins identified as potential interactors with UNC-45a in our screen (Fig. 5 A and Table S1). Importantly, myosin 1c levels were dramatically reduced in UNC-45a knockout cells, whereas protein

A

Uniprot ID	Protein names	UNC-45A-BirA_1 (spectral counts)	UNC-45A-BirA_2 (spectral counts)
Q9H3U1	Protein unc-45 homolog A (UNC45A)	447	446
P60709	β-actin (ACTB)	237	239
P35579	Non-muscle myosin heavy chain IIA (MYH9)	128	120
Q9ULH7	MKL/myocardin-like protein 2 (MKL2)	41	50
O00159	Unconventional myosin-Ic (MYO1C, MM1-β)	26	24
P35580	Non-muscle myosin heavy chain IIB (MYH10)	19	18
P13798	Acylamino-acid-releasing enzyme (AARE)	22	15
Q16643	Drebrin (DBN1)	16	19
P07900	Heat shock protein HSP 90-alpha (HSP90AA1)	20	14
P09493	Tropomyosin alpha-1 chain (TPM1)	15	14

Figure 5. **Myosin 1c is a novel client for the UNC-45a chaperone.** (A) Proximity-dependent BioID screen for UNC-45a interaction partners. Listed are the spectral count values of 10 of the most prominent, in vivo biotinylated proteins by BirA-tagged human UNC-45a in U2OS cells from two independent experiments. Myosin 1c is outlined in green. (Table S1 provides a complete list of in vivo biotinylated proteins by UNC-45a-BirA.) (B) WB analysis of myosin X and myosin 1c protein levels from three independent WT and UNC-45a knockout (KO) cell lysates. GAPDH was probed to demonstrate equal sample loading. (C) Presence of myosin 1c aggregates in WT and UNC-45a knockout cells expressing HA–myosin 1c construct 8 h after MG-132 administration. Fluorescent phalloidin, monoclonal anti–HA antibody, polyclonal antibody against NM-IIA heavy chain, and DAPI were applied to visualize F-actin, myosin 1c, NM-IIA, and nuclei, respectively. Red and yellow arrowheads indicate examples of HA–myosin 1c and NM-IIA containing aggregates, respectively, in UNC-45a knockout cells. Bars, 20 µm.

levels of myosin X, another unconventional myosin not present in the BioID screen, were unchanged in the absence of UNC-45a (Fig. 5 B). Similar to NM-IIA and NM-IIB (Fig. 4 C), myosin 1c also had a tendency to form aggregates in UNC-45a knockout cells after MG-132 treatment (Fig. 5 C).

Collectively, these results reveal that UNC-45a is critical for proper folding of NM-IIA, NM-IIB, and myosin 1c in U2OS cells. In the absence of UNC-45a, a large fraction of those myosins fail to fold properly and are destined for proteasomal degradation. If the function of 26S proteasome is inhibited, the incorrectly folded NM-IIA, NM-IIB, and myosin 1c molecules form large aggregates in the cytoplasm.

UNC-45a depletion inhibits the assembly of bipolar NM-II filaments and filament stacks

We next examined whether, in addition to its protein-folding function, UNC-45a also contributed to the assembly of bipolar myosin II filaments in nonmuscle cells. In those studies,

we primarily used structured illumination microscopy (SIM), which is a powerful approach for studying the organization and dynamics of NM-II filaments in cells (Burnette et al., 2014; Fenix et al., 2016; Beach et al., 2017; Hu et al., 2017).

SIM experiments, in which the NM-IIA motor domain was visualized by the RLC antibody, the rod domain with antibodies against the NM-IIA C-terminal region, and actin filaments by fluorescent phalloidin, confirmed the diminished amount and intensity of the stress fibers in UNC-45a knockout cells compared with WT U2OS cells (Fig. 6 A). Importantly, quantification of NM-IIA filaments near the leading edge of the lamellipodium–lamella interface revealed that UNC-45a knockout cells exhibited more unipolar (motor and rod only) NM-IIA assemblies compared with WT cells (Fig. 6 A, right). The exact molecular nature of the unipolar NM-IIA structures remains to be determined, but they are likely to contain more than two myosin heavy chains and may represent short-lived filamentous-assembly intermediates. Although bipolar (motor–rod–motor) NM-IIA filaments were still able to form in UNC-45a knockout cells, those bipolar filaments failed to form larger NM-II stacks, which are abundant in WT cells (Fig. 6 A). When the SIM results were correlated with the diminished myosin II protein levels in UNC-45a knockout cells versus control cells (Fig. 4 A), it was evident that, although the amount of unipolar NM-IIA structures was slightly increased in UNC-45a knockout cells, the abundance of both bipolar NM-IIA filaments and filament stacks was dramatically diminished in the absence of UNC-45a (Fig. 6 B). Moreover, experiments performed with WT and UNC-45a knockout cells expressing NM-IIA with N-terminal mEmerald and C-terminal mApple fusions demonstrated that, although the intensities of unipolar structures were comparable between WT and knockout cells, the bipolar NM-IIA filaments in UNC-45a knockout cells contained fewer individual myosin-II molecules (Figs. 6, C and D; and Fig. S3 D).

We also applied density-gradient centrifugation (Shutova et al., 2012) to compare the assembly of NM-IIA filaments in control and UNC-45a knockout cells. Consistent with the SIM data, that experiment demonstrated an increase in low–molecular weight NM-IIA assemblies in the knockout cells. In WT extracts, NM-IIA was quite evenly distributed to fractions 3–8, whereas in UNC-45a knockout extracts, NM-IIA mainly concentrated on fractions 2 and 3, corresponding to smaller NM-IIA structures (Fig. 6 E). Together, these data demonstrate that UNC-45a not only catalyzes the folding of myosin heavy-chain molecules but also contributes to the assembly of bipolar NM-II filaments and filament stacks in nonmuscle cells.

UNC-45a TPR domain is dispensable for NM-II folding but important for fine tuning the assembly of contractile stress fibers

To dissect the functions of different UNC-45a domains in stress fiber assembly and NM-II folding, we performed knockout-rescue experiments with various UNC-45a–truncated and mutant constructs (Fig. S4 C). The mutated residues/regions were selected based on a sequence alignment between human UNC-45a and *C. elegans* UNC-45 (Fig. S4D), in which the structural and biochemical properties of various protein motifs have been studied previously (Ni et al., 2011; Gazda et al., 2013).

We first mapped the UNC-45a regions required for myosin folding by expressing UNC-45a–GFP constructs (Figs. 7 B and S5 B) in UNC-45a knockout cells, followed by 26S proteasomal inhibition, and visualization of myosin II aggregates

(Figs. 7 A and S5 A). Automated imaging analysis, in which GFP-positive knockout cells displaying NM-IIA aggregates were scored, revealed that the full-length UNC-45a–GFP construct efficiently rescued the myosin aggregate phenotype. Thus, these aggregates indeed result from the lack of UNC-45a in the cell line and do not arise from off-target effects. In addition, the muscle-specific UNC-45b–GFP prevented the formation of NM-IIA aggregates in UNC-45a knockout cells, indicating that both mammalian UNC-45 isoforms can promote the folding of nonmuscle myosins (Figs. 7 C and S5 C). In agreement with previous studies on ceUNC-45 in *C. elegans* myofibrils (Ni et al., 2011), our rescue experiment revealed that the TPR domain of UNC-45a was dispensable for protecting NM-IIA from aggregation, whereas deletion of the UCS domain (ΔUCS) completely impaired the rescue (Fig. 7, A–C). In contrast to the *C. elegans* work (Ni et al., 2011), however, the UCS domain alone could only partially rescue the myosin aggregation phenotype. Furthermore, although deletion of a conserved loop in the UCS domain of ceUNC-45 completely abrogated the chaperone activity (Gazda et al., 2013), the corresponding mutation (Δ619–647) in UNC-45a, even in a combination with ΔTPR or L134W mutation (corresponding to the L121W that inhibits ceUNC-45 chain formation; Gazda et al., 2013), had no detectable effect on the ability of UNC-45a to prevent myosin II aggregation (Fig. S5, A–C).

Although NM-II folding did not require the presence of the N-terminal TPR domain, which is important for Hsp90 interaction and for the formation of UNC-45 oligomers in vitro, the actin stress fibers appeared slightly abnormal in the rescue cells expressing the ΔTPR–GFP construct. To examine the defects in stress fiber organization and contractility in a more-quantitative manner, we scored the size distributions of vinculin-positive focal adhesions in the knockout-rescue cells. Actomyosin contractility regulates vinculin turnover in focal adhesions and disruption of stress fibers or their contractility results in the lack of large, mature focal adhesions (Choi et al., 2008; Wolfenson et al., 2011; Case et al., 2015). Correspondingly, the UNC-45a knockout cells exhibited predominantly small, nascent adhesions, which is most likely a result of the lack of contractile stress fibers or the decrease in the contractility of the remaining stress fibers, although lack of UNC-45a may also affect the size-distribution of focal adhesion through other mechanisms (Fig. 3 B, bottom). Expression of the full-length UNC-45a–GFP rescued the size distribution of focal adhesions close to the one in WT cells (Fig. 8, A and B). In addition, the aberrant UNC-45a knockout migratory phenotype, as assessed by the random migration velocity (Fig. 2 E), was efficiently restored in UNC-45a knockout cells to WT levels, when the full-length UNC-45a was reexpressed (Fig. S5 E). Consistent with the lack of NM-II chaperone activity and the consequent absence of contractile stress fibers, the construct lacking the C-terminal UCS domain (ΔUCS-GFP) could not rescue the focal adhesion phenotype (Fig. 7 A and Fig. 8, A and B). Interestingly, whereas the construct lacking the N-terminal TPR domain (ΔTPR-GFP) could fully rescue the NM-II aggregation phenotype in cells (Fig. 7, A–C), it was less efficient in rescuing the normal size distribution of focal adhesions compared with the WT UNC-45a. The cells expressing ΔTPR-GFP displayed significantly more of the small (0–0.5 μm) and fewer of the intermediate (1–2 μm) and large (2–4 μm) focal adhesions compared with cells expressing full-length UNC-45a (Fig. 8 B). Moreover, expression of the isolated TPR domain in combination with the ΔTPR-UNC45a
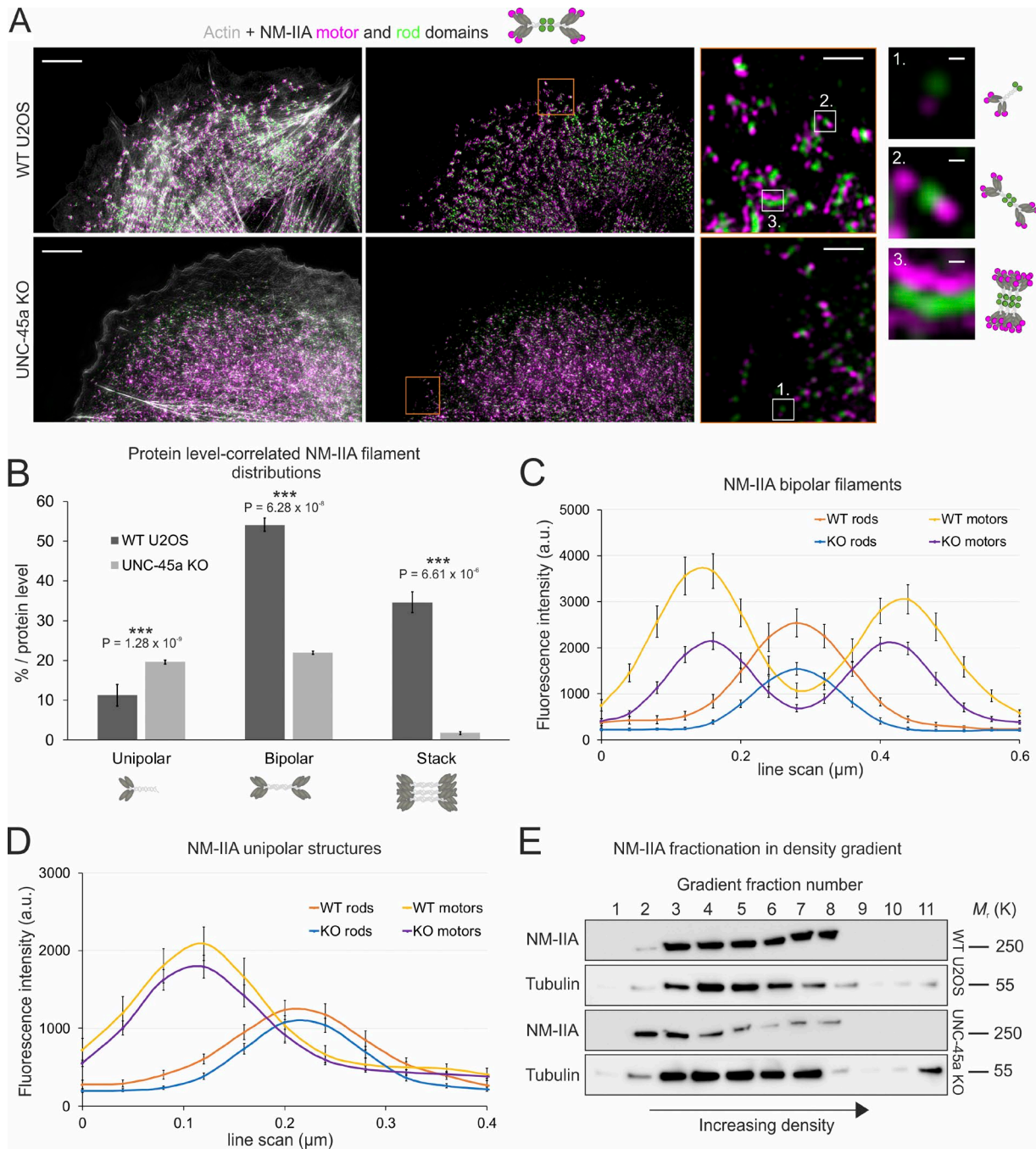
Figure 6. **UNC-45a knockout (KO) cells display defects in formation of bipolar NM-IIA filaments and stacks.** (A) SIM images of representative WT and UNC-45a knockout cells in which actin filaments were visualized by phalloidin. NM-IIA motor domains and tails (rod) were visualized by antibodies against RLC and NM-IIA heavy chain C terminus, respectively. Bars, 5 µm. Magnified regions (corresponding to the orange boxes) display characteristic NM-IIA filament distributions in WT and UNC-45a knockout cells. Bars, 1 µm. High-magnification images of individual filaments (corresponding to the white boxes in the magnified regions) display examples of 1, unipolar structure; 2, bipolar filament; 3, stack of bipolar filaments. Bars, 100 nm. (B) Distributions of different NM-IIA filament populations were quantified from the SIM data, registering all NM-IIA filaments within 2 µm toward the cell body from the first-detected filament at the leading edge. Data obtained on relative percentages of NM-IIA unipolar structures and bipolar filaments were then multiplied by the respective NM-IIA protein levels (WT, 1; knockout, 0. 43; Figs. 4 A and S2 B). n = 261 and 211 NM-IIA filaments analyzed from seven WT and seven UNC-45a knockout cells, respectively. Data are represented as means ± SEM (Student's t test). (C) The fluorescence intensities of bipolar NM-IIA filaments were manually measured from SIM images of WT and UNC-45a knockout cells expressing NM-IIA with N-terminal mEmerald and C-terminal mApple fusions (Fig. S3 D). For the analysis, 16 bipolar filaments were quantified from five control cells, and 22 bipolar filaments were quantified six UNC-45a knockout cells. Data are represented as fluorescence intensity profiles of the motor and rod domains along the line scan length (=x axis); means ± SEM. (D) The fluorescence intensities of unipolar NM-IIA structures were manually measured from mEmerald–NM-IIA–mApple-expressing cells as shown in C. n = 17 and 32 unipolar structures analyzed from five control and six UNC-45a knockout cells, respectively. Data are represented as fluorescence intensity profiles of the NM-IIA motors and rods along the line scan length (=x axis); mean ± SEM. (E) Distributions of NM-IIA molecules in a density gradient. Identical amounts (100 µg) of total cell lysates from WT and UNC-45a knockout cells were subjected to density gradient (0–50%), and a total 11 fractions were collected with increasing density, followed by SDS-PAGE and WB with NM-IIA heavy chain antibody. Tubulin was probed for a fractionation control.
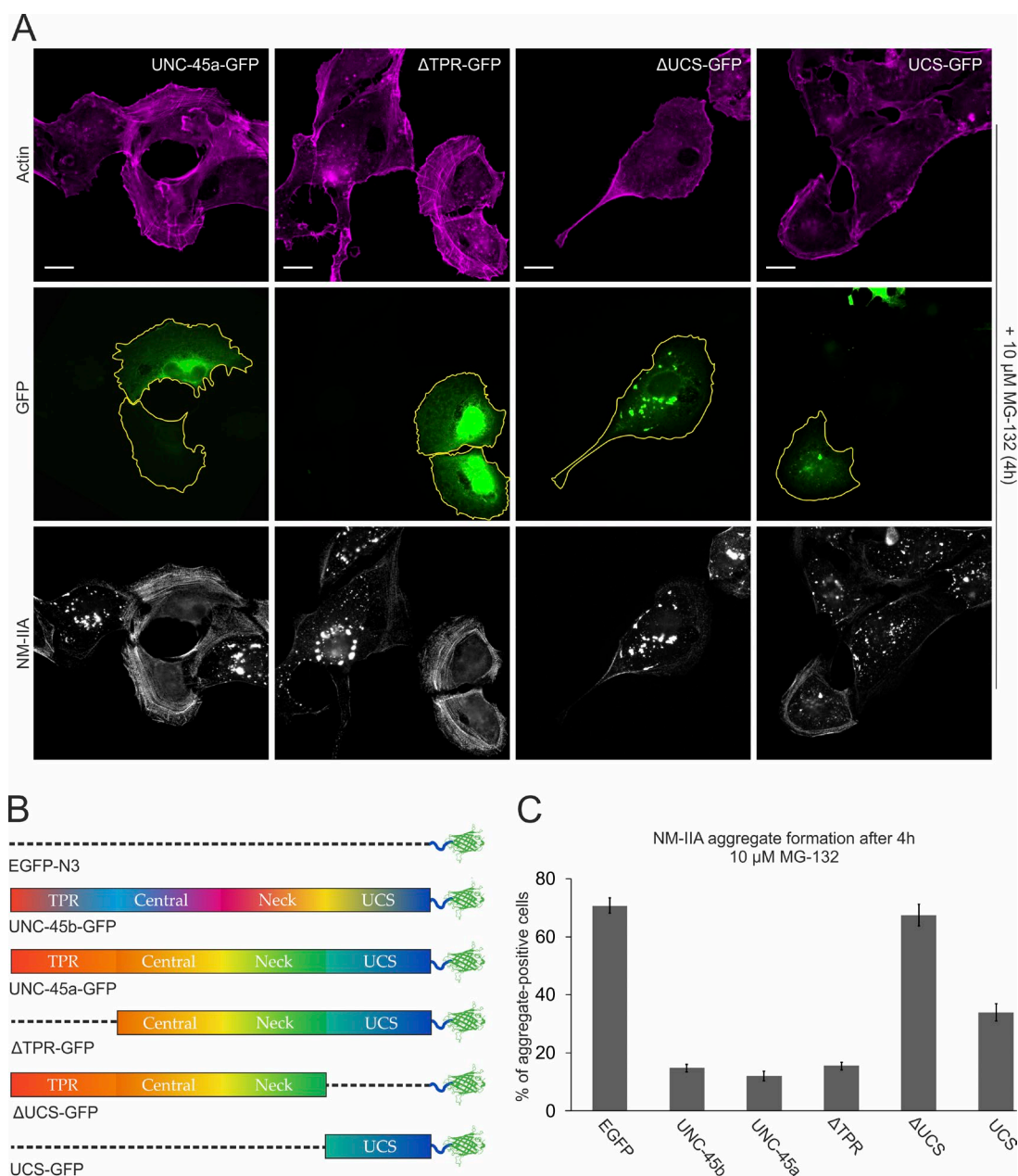
Figure 7. **The UCS domain of UNC-45a is critical for NM-II folding.** (A) Representative examples of UNC-45a knockout cells transfected with different UNC-45-GFP constructs and treated with MG-132 to induce aggregation of misfolded NM-IIA molecules. F-actin and NM-IIA heavy chains were visualized by phalloidin and antibody staining, respectively. The borders of GFP-positive "rescue cells" are highlighted with yellow lines. Bars, 20 μm. (B) Illustration of domain structures of GFP constructs used in the rescue experiments. (C) Quantification of NM-IIA aggregate formation in UNC-45a knockout cells expressing UNC-45b and various UNC-45a constructs after 4-h treatment with 10 μM MG-132 compound. Data are represented as the percentage of transfected cells positive for both GFP and NM-IIA aggregates; means ± SEM; n = 142 for EGFP, 428 for UNC-45b, 330 for UNC-45a, 410 for ΔTPR, 224 for ΔUCS, and 398 for UCS transfected cells.

could not rescue the focal adhesion phenotype further (Fig. S5 D), suggesting that the TPR domain must be covalently linked to the other domains of UNC-45a to facilitate its function in stress fiber contractility.

Together, these results demonstrate that the C-terminal UCS domain is critical for UNC-45a function because of its ability to catalyze NM-II folding. However, UNC-45a appears to use a somewhat different interface that also involves the central domain of the protein for NM-II interactions compared with the ceUNC-45 (Gazda et al., 2013). Our data also reveal that, although the N-terminal TPR domain is dispensable for

NM-II folding, it contributes to the generation of proper contractile stress fibers, probably because of its ability to catalyze the assembly of myosin II filaments through participating in UNC-45a chain formation, as previously reported for ceUNC-45 (Gazda et al., 2013). However, the precise molecular mechanism by which UNC-45a, together with Hsp90, catalyzes myosin folding and filament assembly remains to be resolved.

The role of UNC-45a in cytokinesis

Intriguingly, although the assembly of contractile actomyosin bundles was severely defective in interphase UNC-45a knockout
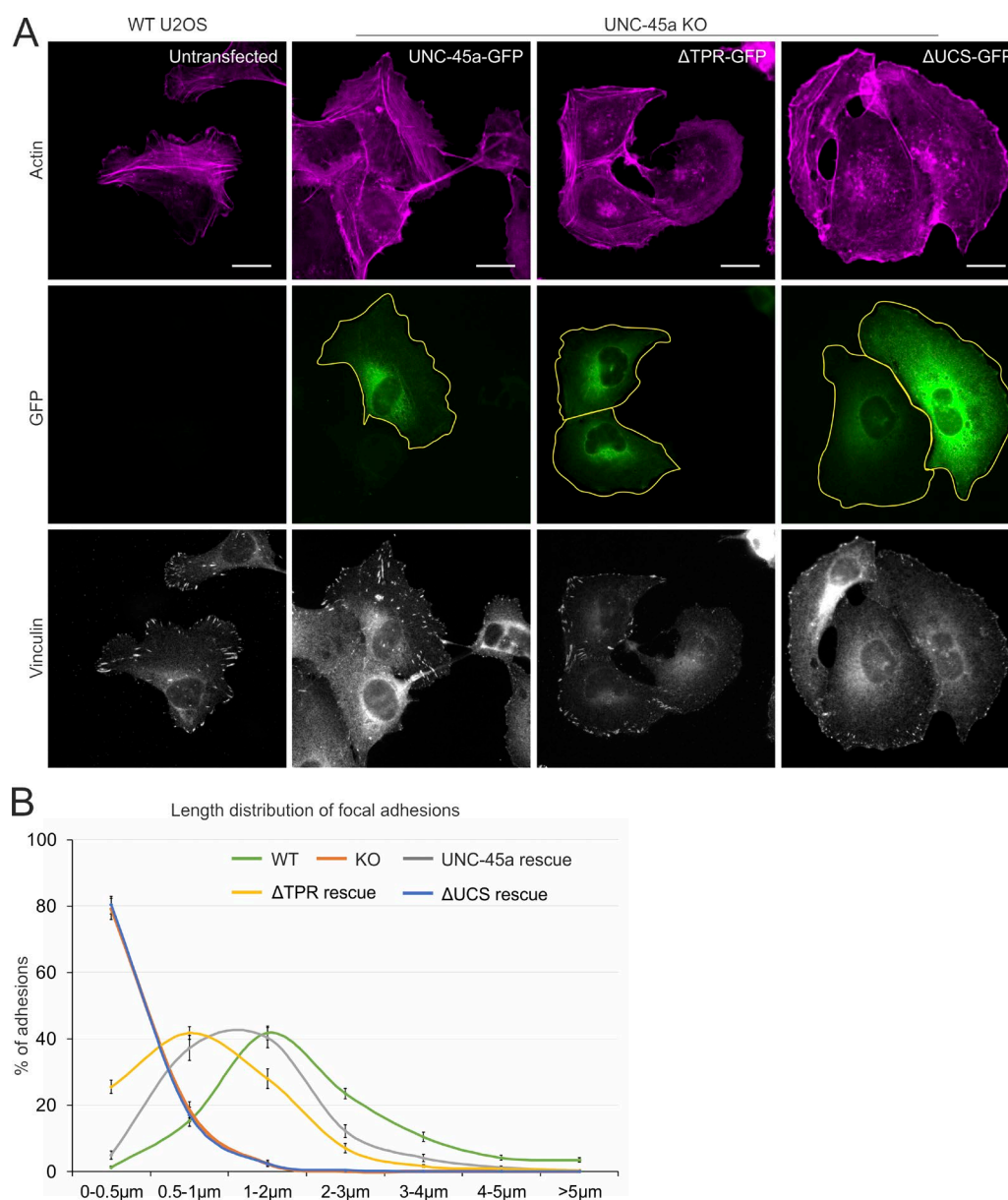
Figure 8. **The TPR domain of UNC-45a contributes to the assembly of contractile actomyosin bundles.** (A) Representative examples of untransfected WT cells and UNC-45a knockout (KO) cells transfected with various UNC-45a–GFP constructs. F-actin and focal adhesions were visualized by phalloidin and by an antibody against vinculin, respectively. The borders of GFP-positive "rescue cells" are highlighted with yellow lines. Bars, 20 µm. (B) The length distributions of vinculin-positive focal adhesions. The number of focal adhesions in each size group was divided by the total focal adhesion number of the same cell. WT, *n* = 1,600 focal adhesions from 25 cells; UNC-45a knockout, *n* = 1,363 focal adhesions from 21 cells; UNC-45a–GFP, *n* = 1,054 focal adhesions from 20 cells; ΔTPR-GFP, *n* = 1,800 focal adhesions from 30 cells; ΔUCS-GFP, *n* = 1,341 focal adhesions from 22 cells. Data are represented as mean ± SEM (Fig. S5 D).

cells, the mitosis phenotype appeared to be less pronounced. An increase in the proportion of multinucleated cells was detected in the absence of UNC-45a (Fig. 9, A and B), and time-lapse imaging revealed slightly delayed cleavage-furrow ingression in UNC-45a knockout cells (Fig. 9, C and D). However, those cells were, in most cases, still able to assemble a NM-II–containing contractile ring and complete cytokinesis, although the NM-IIA filament stack lengths and the amount of NM-II at the division plane were decreased in UNC-45a knockout cells compared with control cells (Fig. 9, E and F). In that context, it is interesting that different cellular actin filament structures may compete for a limited pool of NM-II molecules (Beach et al., 2017). In interphase cells, competition may be stronger because

of the presence of a larger array of NM-II–dependent structures, whereas NM-II in mitotic cells may be mainly concentrated on the contractile ring, without significant competition by other structures. Thus, diminishing the NM-II levels by inactivation of UNC-45a would have a more-pronounced phenotype in stress fibers compared with the contractile ring.

Discussion

NM-II and actin are the main functional elements of contractile actomyosin bundles (i.e., stress fibers) in nonmuscle cells. The mechanisms underlying NM-II folding and self-assembly
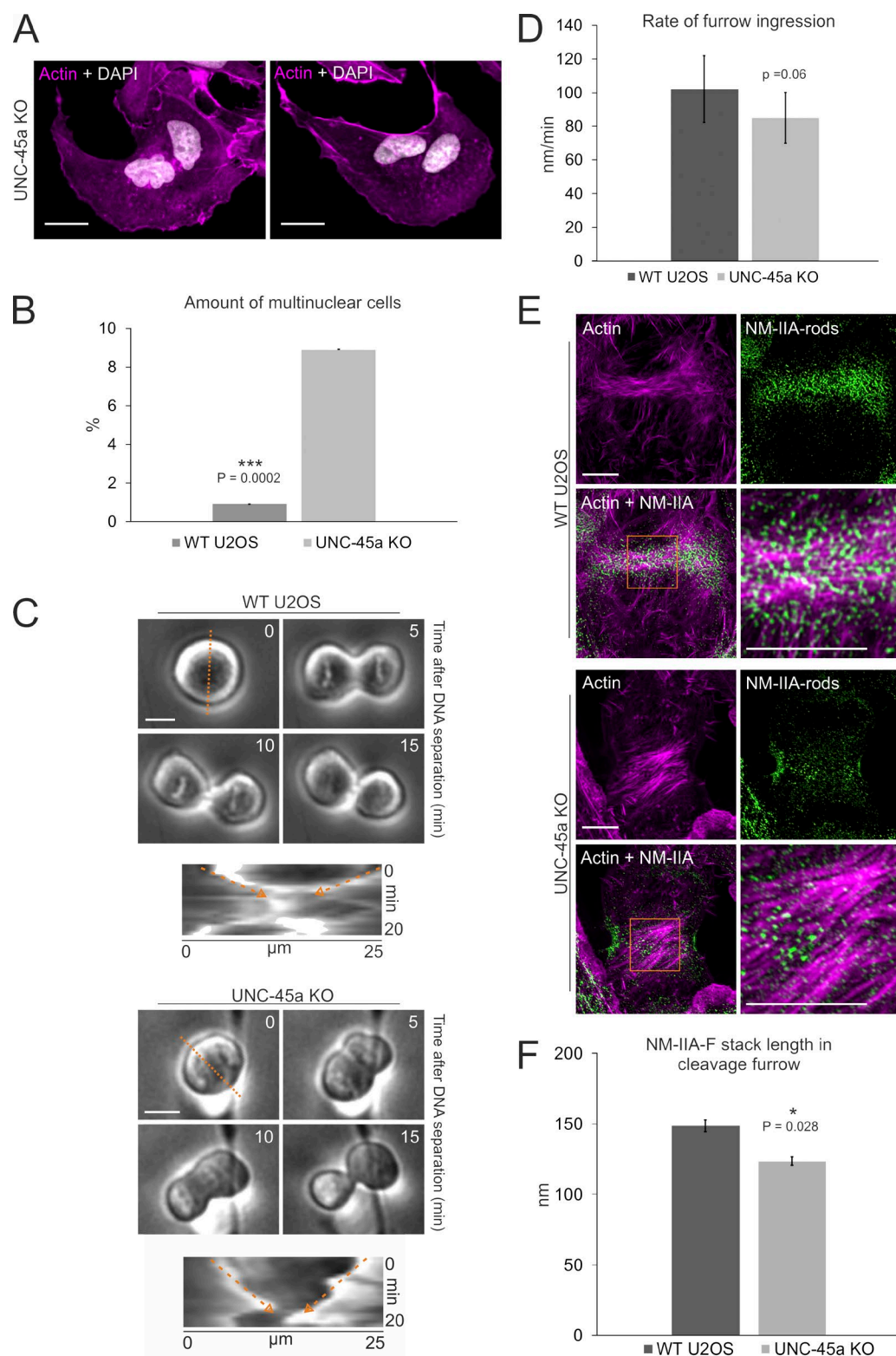
Figure 9. **UNC-45a depletion results in delayed cytokinesis and multinucleated cells.** (A) Visualization of actin and nuclei (DAPI) in UNC-45a knockout (KO) cells. Bars, 20 µm. (B) Quantification of multinuclear WT and UNC-45a knockout cells. Graph displays percentage of multinuclear cells; means ± SEM, WT, $n = 768$ and knockout, $n = 269$ cells. (C) Phase-contrast, time-lapse images on cleavage furrow ingression rates of WT and UNC-45a knockout cells. Time 0 refers to the onset of anaphase. Location of the kymograph is indicated by the orange, dashed line. Orange arrows mark the direction of ingression in the kymograph. Bars, 20 µm. (D) Furrow ingression rate quantification from the phase-contrast, time-lapse data. WT, $n = 31$; UNC-45a knockout, 20 cells from three experiments (Student's t test). (E) SIM images on cleavage furrow of WT and UNC-45a knockout cells with phalloidin-labeled actin filaments (magenta) and NM-IIA rods (green). Magnified views of the ingressing furrow (orange boxes) are displayed on the right. Bars, 5 µm. (F) Quantification of NM-IIA stack lengths in the cleavage furrow of WT and UNC-45a knockout cells. WT, $n = 6$ (1,928 filaments); knockout, $n = 5$ (4,838 filaments) cells. Data are represented as means ± SEM (Mann–Whitney test).

into contraction-competent bipolar filaments as well as their recruitment to the nascent stress fibers are largely unknown (Vicente-Manzanares et al., 2007; Sandquist and Means, 2008; Tojkander et al., 2011, 2015). Here, we reveal that the UNC-45a protein is critical for the assembly of NM-II–containing contractile stress fibers. UNC-45a localizes to stress fibers in a highly dynamic fashion through its conserved C-terminal UCS domain. In the absence of UNC-45a, cells fail to establish proper contractile filaments because of aggregation-prone misfolded NM-II. Moreover, the remaining properly folded NM-II molecules are impaired in forming functional bipolar filaments and stacks. Our knockout-rescue experiments further demonstrate that the C-terminal UCS domain, together with its adjacent regions, is responsible for catalyzing NM-II folding. The N-terminal TPR domain is dispensable for the UNC-45a chaperone function, but it enhances the assembly of contractile actomyosin bundles, suggesting that synchronized NM-II folding and filament assembly occurs in stress fibers via combined activities of UNC-45a UCS and TPR domains, respectively.

To date, the functions of UNC-45 family proteins have been examined primarily in the context of muscle cells, in which depletion of that protein results in drastic defects in myofibril organization (Barral et al., 1998; Venolia et al., 1999; Lee et al., 2011). In contrast, UNC-45 inactivation in invertebrates was not reported to cause major defects in nonmuscle tissues, and depletion of the vertebrate nonmuscle isoform UNC-45a by RNAi or antisense oligonucleotides led to relatively mild phenotypes (Price et al., 2002; Bazzaro et al., 2007; Guo et al., 2011; Comyn and Pilgrim, 2012). However, our results demonstrate that complete depletion of the UNC-45a protein from U2OS cells, which do not express UNC-45b, has a dramatic effect on NM-II homeostasis. The differences in the results between our CRISPR/Cas9 knockout and earlier RNAi/antisense studies might arise from the fact that UNC-45a levels vary among individual cells, and thus, most cells may contain an excess of this myosin II chaperone. Therefore, residual amounts of UNC-45a in RNAi/antisense cells may be sufficient to catalyze NM-II folding, and UNC-45a function can be revealed only if it is completely removed from nonmuscle cells. A small fraction of nonmuscle myosins can still fold properly and assemble into bipolar filaments, even in the complete absence of UNC-45a. The small proportion of bipolar NM-II filaments in UNC-45a knockout cells is likely to result from the contribution of Hsp90 to NM-II folding (Liu et al., 2008).

Our experiments that combined SIM microscopy and proteasome inhibition provided, to our knowledge, the first direct evidence that UNC-45 family proteins contribute to both myosin II folding and to the assembly of functional myosin II filaments within cells. Consistent with earlier studies on invertebrate UNC-45 proteins, the C-terminal UCS domain of UNC-45a is essential for myosin II folding. The N-terminal TPR domain, in contrast, does not contribute to myosin II folding, although it interacts with Hsp90 proteins in vitro (Barral et al., 2002). Instead, our work provides evidence that deletion of that domain leads to mild, yet significant, defects in the proper assembly of contractile stress fibers, most likely because of the role of that domain in enhancing the assembly of bipolar NM-II filaments (Gazda et al., 2013).

We revealed some key differences between UNC-45a and invertebrate UNC-45 proteins. First, although the isolated UCS domain alone is sufficient to rescue the UNC-45–mutant phenotype in *C. elegans* (Ni et al., 2011), the UNC-45a UCS domain could only partially rescue the NM-II–folding phenotype in UNC-45a knockout nonmuscle cells. Interestingly, both central and UCS domains of UNC-45b were shown to bind the myosin II motor in vitro (Bujalowski et al., 2014). Absence of the central domain could thus explain the incomplete clearance of NM-IIA aggregates by the isolated UNC-45a UCS domain. Second, although in ceUNC-45 a Δ602–630 mutation, which discontinues the substrate-binding cleft and abrogates the interaction with myosin, cannot rescue the defect in sarcomere organization (Gazda et al., 2013), the corresponding mutant version of UNC-45a efficiently rescued the NM-II–folding phenotype in U2OS cells. Finally, the dynamics of UNC-45a in actomyosin bundles appears different from the ones reported for muscle UNC-45. In *C. elegans* myofibrils, UNC-45 displayed slow fluorescence recovery in the myosin II–containing A band (Gaiser et al., 2011), whereas our experiments demonstrate that UNC-45a is a dynamic component of NM-II–containing stress fibers. However, UNC-45a displayed a stable association with myosin aggregates, which may be composed of incorrectly folded NM-II molecules (Fig. S1 C). Molecular chaperones are generally regarded as bidirectional, with the greatest affinity to intermediate folding states of the client. In support to that notion, Srikakulam et al. (2008) detected UNC-45b/Hsp90 complex binding only to the unfolded, but not the native, myosin II motor domain in vitro. Thus, rapid dynamics of UNC-45a in stress fibers may ensure that NM-II is associated with UNC-45a only when it is in an unfolded state because, otherwise, UNC-45a would sequester properly folded NM-II.

Why are two, tissue-specific UNC-45 isoforms needed in vertebrates? Although UNC-45b functions in muscle development and cannot be replaced by UNC-45a, UNC-45b can substitute the loss of UNC-45a and colocalize with NM-II in zebrafish embryos (Anderson et al., 2008; Comyn and Pilgrim, 2012; Myhre et al., 2014). In addition, our results show that exogenously expressed UNC-45b can substitute for UNC-45a activity in NM-II folding in human osteosarcoma cells. Biochemical differences between NM-II filaments and muscle myosin II filaments (Liu et al., 2008; Billington et al., 2013; Thoresen et al., 2013) are likely to affect their related chaperone requirements. At a molecular level, UNC-45a may be better suited for initial folding of NM-II during the assembly of relatively dynamic stress fibers. In contrast, muscle-specific ceUNC-45 and UNC-45b are expected to interact primarily with myosin II in myofibrils, which are stable, long-lived structures. Thus, the muscle-specific isoforms may have a major role in repairing damaged myosin II molecules in already-assembled actomyosin bundles, whereas nonmuscle isoforms of UNC-45 may function primarily in initial folding events of NM-II.

In addition to type II myosins, UNC-45a and UNC-45b have additional client proteins. UNC-45b binds the Apo2 protein that is linked to myosepta formation (Etard et al., 2010) and enhances the folding of unconventional myosin-15 in vitro (Bird et al., 2014). UNC-45a was documented to serve as a chaperone for progesterone receptors with Hsp90 (Chadli et al., 2006) and to inhibit retinoic acid receptor signaling (Epping et al., 2009). Functional divergence of these vertebrate muscle and nonmuscle isoforms may have enabled them to adapt to a larger spectrum of substrates (Comyn and Pilgrim, 2012). Compared with invertebrates, vertebrates express a larger repertoire of unconventional myosins; many of which are exclusive to nonmuscle cells (Berg et al., 2001; Odronitz and Kollmar, 2007). Here, we identified unconventional myosin 1c as a novel client

protein for UNC-45a. The lower spectral counts observed in our BioID experiments for myosin 1c and NM-IIB, compared with NM-IIA, may reflect their lower abundances in U2OS cells. Interestingly, the budding-yeast, UCS domain–containing protein She4p/Dim1p was reported to interact with class 1 myosins (myo3p and myo5p; Toi et al., 2003). Class 1 myosins can link the actin cytoskeleton to the plasma membrane and control their mechanical interplay (Raucher and Sheetz, 2000; Nambiar et al., 2009). Lack of correctly folded myosin 1c in UNC-45a knockout cells may thus contribute to the observed aberrant migratory phenotype by lowering the overall membrane tension in the knockout cells. Although our BioID screen efficiently recapitulated the previously published UNC-45a interaction partners NM-IIA, NM-IIB, and Hsp90, we did not detect progesterone receptor or components of the retinoic signaling pathway in the proteomics experiments. Thus, the putative, in vivo role of UNC-45a as a chaperone for those proteins, as well as for other unconventional myosins, remains to be elucidated. Such studies may also shed light on the requirement of two structurally related UNC-45 isoforms in vertebrates.

Materials and methods

Cell culture and transfections

Human osteosarcoma (U2OS) cells, which regularly test negative for mycoplasma with MycoAlert Plus (Lonza), were maintained in high-glucose (4.5 g/l DMEM [BE12-614F; Lonza], supplemented with 10% FBS [10500-064; Gibco], 10 U/ml penicillin, 10 µg/ml streptomycin, and 20 mM L-glutamine [10378-016; Gibco]; later referred to as complete DMEM) at 37°C in humidified atmosphere with 5% CO_2. Transient transfections were performed with Fugene HD (Promega), according to manufacturer's instructions using 3.5:1 Fugene/DNA ratio and 24 h incubation before fixation with 4% PFA in PBS for protein-localization studies. 48-h incubation before fixation was used for rescue experiments. For live cell and SIM imaging, cells were detached 24 h after transfection with Trypsin-EDTA (0.25% wt/vol) and plated onto glass-bottomed, 10 × 35-mm dishes (Greiner Bio-One), coated with either 10 µg/ml fibronectin (Roche) or 25 µg/ml laminin (L2020; Sigma-Aldrich) diluted in PBS. siRNA experiments were performed with INTEFERin (PolyPlus Transfection), according to manufacturer's instructions, using 40 nM Hs_SMAP1_4 siRNA (target sequence, 5′-CCGGGCCGCCTGCCACCTCAA-3′; QIAGEN) or 40 nM AllStars negative-control siRNA (QIAGEN). A 72-h incubation period was used to efficiently deplete the target protein. Proteasome inhibition was conducted with 10 µM MG-132 (Abcam), dissolved from 10 mM stock (in DMSO) directly to complete DMEM at 37°C. Cells were fixed with 4% PFA for 4 or 8 h after administration of the drug.

Plasmids

Full-length human UNC-45a coding sequence (available from GenBank under accession no. NM_018671.3) in pENTR221 vector (ORFeome Library; Biocentrum Helsinki Genome Biology Unit) was cloned into the EGFP-N1 backbone (Takara Bio Inc.) with EcoRI and KpnI restriction sites. TPR–mRuby2 (residues 1–146), ΔTPR–GFP (residues 147–971), ΔUCS–GFP (residues 1–539), and UCS–GFP (residues 540–971) were produced by PCR from UNC-45a cDNA, including the ATG start codon, and subcloned into mRuby2-N1 (54614; a gift from M. Davidson, Addgene, Cambridge, MA; Lam et al., 2012) and the EGFP-N3 vector (Takara Bio Inc.), respectively. L134W–Δ619–647 and ΔTPR–Δ619–647 double mutations were introduced to UNC-45a–GFP and ΔTPR–GFP plasmids, respectively, using one-step, site-di-

rected mutagenesis (Liu and Naismith, 2008). L134W point mutation was introduced first, followed by the deletion of the 28-residue loop in UCS (Δ619–647). Human UNC-45b coding sequence was purchased from DNASU Plasmid Repository (HsCD00505951) and cloned into EGFP-pDEST-N3 vector (a gift from M. Vartiainen, University of Helsinki, Helsinki, Finland). GFP–NM-IIA plasmid was a gift from R. Adelstein (11347; Addgene, Cambridge, MA; Wei and Adelstein, 2000). Cloning of mApple–NM-IIA (mApple–myosin-IIA–C-18) and mEmerald–NM-IIA–mApple (mEmerald–C-16–mApple–N-14–myosin-IIA) are described in Burnette et al. (2014). UNC-45a–paGFP and NM-IIA–paGFP were both constructed by restriction cloning using a paGFP–N3 vector (a gift from M. Vartiainen) with EcoRI–KpnI and HindIII–KpnI sites, respectively. HA–myosin 1c construct was a gift from M. Vartiainen. Myosin 1c (isoform B) cDNA was cloned into an EGFP–C1 vector (Takara Bio Inc.) with GFP replaced with the HA-tag.

Reagents

Polyclonal mouse antibody (H00055898-B01P) against full-length recombinant human UNC-45a was purchased from Abnova (1:125 dilution for IF analysis; 1:300 dilution for WB). Paclitaxel (T7402) and rabbit polyclonal phospho-myosin (Thr18, Ser19) RLC (3674) were purchased from Cell Signaling Technology (1:200 IF). 100 mg/ml cycloheximide (1:1,000; C4859), monoclonal mouse antibody (V9131) against full-length human vinculin, (1:700 IF; 1:1,000 WB), mouse monoclonal (M4401) anti–RLC (1:200 IF; 1:1,000 WB), polyclonal rabbit UNC-45b (HPA017861) recognizing 114 C-terminal residues (1:250 WB), monoclonal mouse β-actin (A5441) recognizing the N terminus of protein (1:10,000 WB), mouse monoclonal antibody (T5168) against the α-tubulin C terminus (1:10,000 WB), mouse monoclonal anti–HA antibody (H9658; 1:1,000 IF), and rabbit polyclonal antibody recognizing human myosin 1C (HPA001768) residues 247–394 (1:2,000 WB) were purchased from Sigma-Aldrich. Rabbit polyclonal (ab73412) recognizing the vinculin C terminus (1:200 IF), mouse monoclonal (ab684) against the C-terminal tail (1964–1976) of NMHC-IIB (1:100 IF), rabbit monoclonal (ab183734) recognizing full-length GFP (1:10,000 WB), mouse monoclonal (ab53497) against full-length Hsp90β protein (1:1,000 WB), and rabbit polyclonal antibody (PAB1195) recognizing the full-length GAPDH (1:10,000 WB), and the human skeletal muscle-tissue total lysate (ab29330) were purchased from Abcam. Polyclonal NMHC-IIA antibody (909801) binding to the C-terminal tail residues 1948–1960 (1:1,000 IF and WB) and NMHC-IIB antibody (909901) binding to residues 1965–1976 in the C terminus (1:100 IF, 1:400 WB) were purchased from BioLegend. Polyclonal rabbit myosin-X antibody (22430002; 1:1,000 WB) was purchased from Novus Biologicals. Pageruler Plus protein ladder (26619); DAPI (D1306; 1:10,000 IF); phalloidin (P3457); Alexa Fluor phalloidin 488 (A12379) and 568 (A1238; 1:100 IF); Alexa Fluor goat anti–mouse 488 (A11001), 568 (A11004), and 647 (A31571); Alexa Fluor goat anti–rabbit 488 (A11034) and 647 (A21245; all 1:200–1,000 IF); and both HRP-conjugated goat anti–rabbit (G-21234) and HRP-conjugated goat anti–mouse (G-21040; both 1:5,000 WB) antibodies were purchased from Thermo Fisher Scientific.

CRISPR construct design

Guide sequence targeting exon 7 of the human *UNC45a* gene was selected based on the CRISPR Design Tool, with a quality score of 91, targeting both UNC-45a splice variants (Guo et al., 2011). Oligonucleotides for cloning guide RNA into pSpCas9 (BB)-2A-GFP vector (48138; a gift from F. Zhang, Addgene, Cambridge, MA) were designed as described previously (Ran et al., 2013). Transfected cells were detached 24 h after transfection, suspended into complete DMEM with 20 mM Hepes, and sorted with FACSAria II (BD), using low-intensity,

GFP-positive pass gating, as single cells onto a 96-well plate, supplemented DMEM containing 20% FBS and 10 mM Hepes. CRISPR clones were cultivated for 2 wk before selecting clones with no discernible UNC-45a protein expression. Of six total surviving clones screened, which exhibited identical phenotypes and no detectable UNC-45a protein expression, one was selected for use in this study.

IF microscopy

Cells were fixed with 4% PFA PBS, followed by extraction with 0.1% Triton X-100 in PBS that included DAPI. For SIM, 4% PFA PBS fixed cells were extracted with 1% Triton X-100 in 4% PFA PBS. Cells were blocked in 1× Dulbecco PBS supplemented with 0.2% BSA. Live-cell extraction (5× stock solution containing 500 mM Pipes, 25 mM ethylene glycol tetra-acetic acid [pH 6.9], 25 mM MgCl₂, 10% polyoxyethylene glycol [35,000 mol wt], 5% Triton X-100, 10 µM paclitaxel, and 10 µM phalloidin) for removal of cytoplasmic, unbound proteins was performed as previously described (Burnette et al., 2011; Fenix et al., 2016). Both primary and secondary antibodies diluted with Dulbecco's PBS were applied onto cells, incubated at RT in a dark, humified chamber, and washed 3 times with Dulbecco's PBS. Alexa-conjugated phalloidin was added, along with primary antibodies. Samples were mounted in Mowiol, containing 2.5% wt/vol 1,4-diazabicyclo[2.2.2]octane (Sigma-Aldrich). For SIM, cells were blocked in 10% BSA in PBS, and both primary and secondary antibodies were diluted to 10% BSA PBS. Vectashield H-1000 (Vector Laboratories) was used for mounting. All IF data were obtained with DM 6000B (Leica Biosystems) and Application Suite X software (Leica Biosystems) using 63×/1.40-0.60 HCX PL Apochromat objective, and Semrock Brightline filters: DAPI-5060C (excitation [ex], 377/50; emission [em], 447/60), GFP-4050B (ex, 466/40; em, 525/50), TRITC-B (ex, 543/22; em, 593/40), Cy5-4040C (ex, 628/40; em, 692/40), with an Orca-Flash4.0 V2 scientific complementary metal-oxide semiconductor (sCMOS) camera (Hamamatsu Photonics).

Real-time quantitative PCR

Total mRNA was extracted with the GeneJET RNA purification kit (K0731; Thermo Fisher Scientific) and single-stranded cDNA was synthesized (K1671; Thermo Fisher Scientific) from 500 ng of extracted mRNA. Primers amplifying a 200-bp region common to all known isoforms of *MYH9*, *MYH10*, and *GAPDH* (with one of the primers for each gene hybridizing to an exon–exon junction), were designed with the Primer-BLAST tool (Ye et al., 2012). Quantitative PCR reactions were performed with Maxima SYBR Green/ROX (K0221; Thermo Fisher Scientific) in Bio-Rad Laboratories CFX96. Changes in expression levels were calculated with the $2^{-\Delta\Delta Ct}$ method, normalized to GAPDH (ΔCt) and WT expression levels, respectively.

Photoactivation and live cell imaging

For photoactivation experiments, U2OS cells transfected with UNC-45a/NM-IIA–paGFP and mApple–NM-IIA constructs were trypsinized 24 h after transfection, plated, and imaged on fibronectin-coated, glass-bottomed, 35-mm dishes (Greiner Bio-One) in complete DMEM supplemented with 10 mM Hepes. Culture dishes were placed in a 37°C sample chamber with controlled 5% CO₂ flow, and time-lapse photoactivation data were acquired with 3I Marianas (Intelligent Imaging Innovations), equipped with an Axio Observer Z1 (ZEISS), CSU-X1-M1 confocal scanner (Yokogawa), Brightline filters (Semrock), and a Neo sCMOS camera (Andor), using 63×/1.2W C-Apochromat Corr WD of 0.28, M27 objective. Imaging sequence of 1-ms activation using 5% (405 nm) laser power followed by 1-s imaging intervals on 488 and 561 channels was set up with Slidebook 6 (Intelligent Imaging Innovations). Activation spots (except for cytosolic

activation) were selected on the most-prominent stress fibers with the width of the mApple–NM-IIA signal used as borders for the activation area. For data analysis, depletion of both extraneous and cytosolic background fluorescence was followed by normalization of each time-lapse experiment intensity values to the activation-point intensity. For figure generation, UNC-45a-photoactivation time-lapse images were deconvolved using the 2D nonblind option in Autoquant X3 software (Media Cybernetics) to improve resolution. Phase contrast and 488-GFP time-lapse imaging were conducted on a continuous cell-culturing platform Cell-IQ (CM Technologies). 6-well plates (Greiner Bio-One) were coated with laminin, and the plate lid was switched to Cell-Secure (CM Technologies), enabling insertion of CO₂ input and output valves. Cells were allowed to attach for 2 h, washed twice with PBS, and replaced with complete DMEM containing 10 mM Hepes before starting the imaging. Mean migration velocity of WT and knockout cells was quantified by tracking the movement of nuclei for 10-min (20 min for UNC-45a–GFP rescues) imaging cycles for 10 h (6–10 h for UNC-45a–GFP rescues) with Cell-IQ Analyser (CM Technologies). Only cells that were not colliding with one another were selected for measurements. Cell length was measured as a distance from the edge of the nucleus to the plasma membrane of furthest intact part of the cell edge with the ImagePro Analyzer (Media Cybernetics). Lamellipodial protrusions were determined by counting the numbers of persistent, simultaneous protrusions (extending throughout one imaging cycle). This was crucial to distinguish between protruding and stationary or weakly retracting parts of cells. Protrusion profile was calculated for all cells on each of the eight imaging cycles and averaged for WT and knockout cells respectively.

Western blotting

Cell lysates were prepared by washing cells with PBS and scraping into lysis buffer (50 mM Tris-HCl, pH 7.5, 150 mM NaCl, 1 mM EDTA, 10% glycerol, 1% Triton X-100, supplemented with 1 mM PMSF, 10 mM DTT, 40 µg/ml DNase I, and 1 µg/ml of leupeptin, pepstatin A, and aprotinin), followed by a brief sonication. All preparations were conducted at 4°C. Protein concentrations were determined with Bradford reagent (500-0006; Bio-Rad Laboratories) and equal amounts of the total cell lysates mixed and boiled with Laemmli Sample Buffer were loaded and run on 4–20% gradient SDS-PAGE gels (4561096; Bio-Rad Laboratories). Proteins were transferred to nitrocellulose membrane with Trans-Blot Turbo (Bio-Rad Laboratories). Membrane was blocked in 5% milk/BSA-TBS with 0.1% Tween 20, and incubated overnight at 4°C and 1 h at RT with primary and secondary HRP-conjugated antibodies, respectively, diluted in fresh blocking buffer. Proteins were detected with Western Lightning ECL Pro substrate (PerkinElmer). All band-intensity quantifications were conducted with ImageJ (Schneider et al., 2012) densitometry analysis and normalized to either tubulin or GAPDH protein levels.

Density-gradient fractionation

NM-IIA fractionation was performed as described by (Shutova et al., 2012). In brief, cells were scraped from 60-mm cell culture dishes into lysis buffer and centrifuged 68,000 rpm in TLA-120.2 (Beckman Coulter). Soluble protein fraction was measured with a Bradford assay and identical amounts (100 µg) of total cell lysates were applied on the top of discontinuous Optiprep density gradient (D1556; Sigma-Aldrich) consisting of (from bottom to top) 50, 25, 12, and 6% layers in lysis buffer, and centrifuged at 80,000 rpm. 11 fractions were collected straight into the Laemmli Sample Buffer, separated with SDS-PAGE, transferred to nitrocellulose membrane, and probed with NMHC-IIA and tubulin antibodies.

SIM

SIM imaging was performed at RT on a GE Healthcare DeltaVision OMX Super Resolution microscope equipped with a sCMOS camera (512 × 512), a 60× Plan-Apochromat N/1.42 NA oil objective, and 405, 488, 568, and 642 laser lines. Samples were plated on, and imaged in, 35-mm, glass-bottom dishes (Cellvis). Displayed images represent 3D reconstructions, as described elsewhere (Gustafsson, 2005). Final images have a pixel size of 40 µm. Imaging and reconstruction was performed as in Fenix et al. (2016).

High-content screening

Untransfected and transfected knockout cells and WT cells were plated onto 96-well ViewPlates (PerkinElmer). 48 h after plating, cells were treated with MG-132 for 4 h and fixed. Quadruplicate wells were stained with DAPI, phalloidin 568, and NMHC-IIA. For each cell line and transfectant, control wells with only phalloidin or NMHC-IIA staining were included to normalize bleed through. Plates were imaged with CellInsight (Thermo Fisher Scientific) using an Olympus 20× NA, 0.4 objective, and a charge-coupled device camera with the following light-emitting diode ex: 386 ± 23, 485 ± 20, 549 ± 15, and 630 ± 13 nm. Automated imaging in room temperature was conducted, acquiring 20 images from each well using DAPI signal for autofocus. Images from CellInsight high-content screening were analyzed with CellProfiler 2.1.1 (Kamentsky et al., 2011) software and classified into phenotypes with Advanced Cell Classifier 2.0 software (Horvath et al., 2011). In CellProfiler, nuclei were first segmented from the DAPI channel and used as seeds to propagate the whole-cell segmentation using the phalloidin channel. The segmented cells were applied to measure various intensity-based features from the GFP, myosin, and phalloidin channels, as well as texture features from the myosin channel. Altogether 105 features were extracted from each cell and imported to Advanced Cell Classifier for supervised machine learning. Advanced Cell Classifier was used to train a multiparametric model separately for every experiment. In total, six classes were defined: GFP⁻ WT, GFP⁻ knockout, GFP⁻ (cells with) dots, GFP⁺ WT, GFP⁺ knockout, and GFP⁺ (cells with) dots. Both the GFP⁻ and GFP⁺ dot data were used for assembling Figs. 7 C and S5 C. For each experiment, an expert annotated ~50 (16–70) cells into each class. The annotated cells were used to train the Random Forest classifier (Breiman, 2001), which was used to automatically predict the phenotypes of all cells.

Phase microscopy and ingression rate quantification

Live-cell, wide-field phase microscopy videos were acquired on a Nikon Eclipse Ti, equipped with a Nikon 20× Plan 0.40 NA air objective and a DS-Qi2 complementary metal-oxide semiconductor camera. Images were acquired every 1 min. Cells in DMEM supplemented with 10 mM Hepes, were placed in a Tokai Hit stage-top incubation system during imaging at 37°C and 5% CO₂, and an orange, glass filter was placed on top of the condenser to restrict short wavelengths of light. Rates of ingression were calculated using ImageJ. Images were first aligned using the "StackReg" plugin, and a line of width 3 was drawn across the division plane of the dividing cells. Kymographs were generated using the "MultipleKymograph" plugin in ImageJ. Rates of ingression were then manually calculated from when the cell started to ingress until ingression had stopped, resulting in distance over time measurements.

NM-IIA filament population distribution and cleavage furrow stack-length quantification

Quantification of NM-IIA filament population distribution from the SIM data was conducted as described in Fenix et al. (2016) with the following modifications: 2-µm-wide area of the lamellum was drawn with ImageJ, starting from the most distal NM-IIA filament detected along the cell edge. All unipolar and bipolar filaments and stacks were manually quantified within that area. Fiji and Slidebook 6 were used for quantification of NM-IIA stack lengths in the cleavage furrow. All data used for quantification were acquired on a SIM (Deltavision OMX; GE Healthcare). A 12 × 7-µm box (determined empirically as the best size for all cells measured) was placed in the middle of the cleavage furrow, and every NM-IIA filament was measured as in Fenix et al. (2016). Thus, for every image, the length of each filament and the number of total filaments were quantified, allowing stack-length quantifications.

BioID screen

BirA from pmycBioID-C1 (a gift from J. Peränen, University of Helsinki, Helsinki, Finland), together with either full-length human UNC-45a (cloned from UNC-45a-GFP) or EGFP (EGFP-N3) cDNA, was cloned into pcDNA4/TO vector (Thermo Fisher Scientific). An HA tag, introduced as a linker between the cDNA and BirA, was used as a complementary sequence to fuse the corresponding cDNA and BirA together in a nested PCR reaction and was further amplified in later cycles with the primers binding the 5′ and 3′ terminal ends of the fusion construct. The UNC-45a–HA–BirA and BirA–HA–EGFP constructs obtained were transfected to the U2OS cell line stably expressing pcDNA6/TR (a gift from M. Vartiainen) and were grown in complete DMEM with 300 µg/ml Zeocin and 2.5 µg/ml blasticidin A (Invivo-Gen) to select and establish tetracycline-inducible clones. Expression of the constructs was verified by staining clones, which were either untreated or treated for 24 h with 2 µg/ml tetracycline in complete DMEM with an anti–HA antibody. Four clones (two for both constructs) displaying strong induction after tetracycline addition were expanded to 15-cm tissue-culture plates and treated with 2 µg/ml tetracycline and 50 µM biotin in complete DMEM. Cells were harvested 24 h after the induction and washed three times with PBS. Cell pellet was snap frozen in liquid NO₂ and stored at −80°C. Cell pellets were lysed on ice for 10 min in HNN buffer, supplemented with 0.5% NP-40, 1.5 mM Na3VO4, 1.0 mM PMSF, 10 µl/ml protease inhibitor cocktail (Sigma-Aldrich), 0.1% SDS, and 80 U/ml Benzonase Nuclease (Santa Cruz Biotechnology, Inc.). Incubation was followed by three cycles of sonication. Lysate was centrifuged twice at 16,000 g at 4°C to remove the insoluble material. During centrifugation, Bio-Spin chromatography columns (Bio-Rad Laboratories) were loaded with Strep-Tactin sepharose beads (400 µl 50% slurry; IBA Lifesciences) and washed once with 1-ml HNN buffer containing 0.5% NP-40 and inhibitors (HNN wash buffer). Cleared lysate was loaded on spin columns, followed by three washes with ice-cold HNN wash buffer and four washes with ice-cold HNN buffer without supplements. Bound proteins were eluted with 2 × 300-µl freshly prepared 0.5 mM D-biotin (Thermo Fisher Scientific) in HNN buffer into a fresh 2-ml tube.

Mass spectrometry

For liquid chromatography–tandem mass spectrometry, samples were prepared as follows: cysteine bonds were reduced with 5 mM Tris (2-carboxyethyl) phosphine (Sigma-Aldrich) at 37°C and alkylated with 10 mM iodoacetamide (Fluka; Sigma-Aldrich) at RT in the dark. A total of 1 µg trypsin (Promega) was added, and samples were digested overnight at 37°C. Samples were quenched with 10% trifluoroacetic acid (TFA) and purified with C-18 Micro SpinColumns (The Nest Group) eluting the samples to 0.1% TFA in 50% acetonitrile. Samples were dried by vacuum concentration, and peptides were reconstituted in 30 µl buffer A (0.1% TFA and 1% acetonitrile in LC-MS grade water) and vortexed thoroughly.

Liquid chromatography–tandem mass spectrometry analysis was performed on an Orbitrap Elite electron transfer dissociation hybrid mass spectrometer using the Xcalibur (version 2.2, SP 1.48) coupled

to the EASY-nLCII system (all from Thermo Fisher Scientific) via a nanoelectrospray ion source. 5 µl of peptides was loaded from BioID samples. Samples were separated using a two-column setup consisting of a C18 trap column (EASY-Column, 2 cm × 100 µm, 5 µm, 120 Å; Thermo Fisher Scientific), followed by C18 analytic column (EASY-Column 10 cm × 75 µm, 3 µm, 120 Å; Thermo Fisher Scientific). Peptides were eluted from the analytic column with a 60-min linear gradient from 5 to 35% buffer B (buffer A, 0.1% FA, 0.01% TFA in 1% acetonitrile; buffer B, 0.1% FA, 0.01% TFA in 98% acetonitrile). Analysis was performed in data-dependent acquisition mode, in which a high-resolution (60,000) Fourier transform mass spectrometer full scan (mass-to-charge ratio, 300–1700) was followed by top-20 (20 most-abundant ions) Collision-induced dissociation tandem mass spectrometry spectra (CID-MS^2) scans in ion trap. The SEQUEST search algorithm in Proteome Discoverer software (Thermo Fisher Scientific) was used for peak extraction and protein identification with the rat reference proteome of the UniProtKB/SwissProt database (www.uniprot.org). Allowed error tolerances were 15 parts per million and 0.8 D (difference) for the precursor and fragment ions, respectively. Database searches were limited to fully tryptic peptides, allowing one missed cleavage (in peptide mapping, semitryptic with one missed cleavage allowed); carbamidomethyl +57,021 D (C) of cysteine residue was set as fixed, and oxidation of methionine at +15,995 D (M) was set as dynamic modifications. For peptide identification, the false discovery rate was set to <0.05. The high-confidence protein interactions were identified using stringent filtering against GFP control runs.

Focal adhesion data quantification

Focal adhesion lengths were manually quantified from untransfected, WT, knockout, and mutant UNC-45a–GFP rescue cells with ImageJ, measuring each individual adhesion size with the ROI Manager and straight-line tools in ImageJ. Cells that adhered to several neighbors were discarded from the analysis. From transfected cells, only those displaying low or moderate GFP intensity were selected for analysis. Adhesion was classified into seven size groups and the percentual ratio of the focal adhesion in each class was obtained by dividing the focal adhesion number of individual size classes with the total number of focal adhesions in the same cell.

Primers used in this study

Both forward (F) and reverse (R) primers used in this study are presented. Complementary sequences to the target cDNAs are underlined, except for quantitative PCR oligonucleotides and for the L134W and Δ619–647 oligonucleotides that were designed based on Liu and Naismith (2008).

Cloning primers for UNC-45a-GFP and UNC-45a-GFP mutants and paGFP. UNC-45a F: 5′-GTAGTAGAATTC<u>ATGACTGTGAGTGGTCCAGG</u>-3′, UNC-45a R: 5′-GTAGTAGGTACCTT<u>CTCTCCATCTTGGTTGGGTT</u>-3′; TPR F: 5′-GTAGTAGAATTC<u>ATGACTGTGAGTGGTCCAG</u>-3′, TPR R: 5′-GTAGTAGGTACCAA<u>TCGCACCTTCTCCTGAATC</u>-3′; ΔUCS F: 5′-GTAGTAGAATTCATGACT GTGAGTGGTCCAGG-3′, ΔUCS R: 5′-GTAGTAGGTACC<u>GGAGCCTTCAGCAAACTGC</u>-3′; ΔTPR F: 5′-GTAGTAGAATTCATG<u>TACATGTCCTCGACGGATGC</u>-3′, ΔTPR R: 5′-GTAGTAGGTACCTT<u>CTCTCCATCTTGGTTGGGTTG</u>-3′; UCS F: 5′-GTAGTAGAATTCATG<u>ACTCTCAAACTGGCTAAGCAGTGTC</u>-3′, UCS R: 5′-TAGTAGGTACC<u>CTCTCCATCTTGGTTGGGTTG</u>-3′; L134W F: 5′-AAGTTTTCCAGGAGGCCTGGCGGAACATCGG-3′, L134W R: 5′-CCGATGTTCCGCCAGGCCTCCTGGAAAACTT-3′; Δ619-647 F: 5′-TGGTGAACTGCACCAACAAGCCAAGCTTCGTGCGGGC-3′, Δ619-647R: 5′-GCACGAAGCTTGGCTTGTTGGTGCAGTTCACCAGCGCTG-3′; UNC-45a-paGFP F: 5′-GTAGTAGAATTC<u>ATG</u>

<u>ACTGTGAGTGGTCCAGG</u>-3′, UNC-45a-paGFP R: 5′-GTAGTA GGTACC<u>CTCTCCATCTTGGTTGGGTT</u>-3′; NM-IIA-paGFP F: 5′-GTAGTAAAGCTT<u>ATGGCACAGCAAGCTGC</u>-3′, NM-IIA-paGFP R: 5′-TACTACGGTACC<u>TTCGGCAGGTTTGGCCTC</u>-3′.

Guide RNA oligonucleotides for CRISPR, targeting exon 7 of human UNC-45a. e7_hsUNC45a F: 5′-CACC<u>ATGTCAAAGCACTCTACCGG</u>-3′; e7_hsUNC45a R: 5′-AAAC<u>CCGGTAGAGTGCTTTGACATC</u>-3′.

UNC-45a-HA-BirA cloning primers for the BioID screen. KpnI-UNC45a F: 5′-GTAGTAGGTACC<u>ATGACTGTGAGTGGTCCAGGG</u>-3′; UNC-45a-HA R: 5′-GGCGTAGTCAGGCACGTCGTAAGGATA<u>CTCTCCATCTTGGTTGGGTTG</u>-3′; HA-BirA F: 5′-TATCCTTACGACGTGCCTGACTACGCC<u>ATGGAACAAAAACTCATCTCAGAAGAG</u>-3′, BirA-EcoRI R: 5′-GTAGTA GAATTC<u>TCACTTCTCTGCGCTTCTCAG</u>-3′.

BirA–HA–EGFP cloning primers for the BioID screen. KpnI-BirA F: 5′-GTAGTAGGTACC<u>ATGGAACAAAAACTCATCTCAGAAGAG</u>-3′; BirA-HA R: 5′-GGCGTAGTCAGGCACGTCGTAAGGATA<u>CTTCTCTGCGCTTCTCAGGG</u>-3′; HA-EGFP F: 5′-TATCCTTACGACGTGCCTGACTACGCC<u>ATGGTGAGCAAGGGCGAG</u>-3′, EGFP-EcoRI R: 5′-GTAGTAGAATTC<u>TTACTTGTACAGCTCGTCCATGCC</u>-3′.

Quantitative PCR oligonucleotides for *MYH9*, *MYH10*, and *GAPDH*. *MYH9* F: 5′-CTATCCGCCAAGCCAAGGAA-3′,

MYH9 R: 5′-GCCCATAATCCTCATGGCCT-3′; *MYH10* F: 5′-CAAATCGAGGCTGCGAACAA-3′, *MYH10* R: 5′-GAGGCAAGTTCCTCCTGCAA-3′; *GAPDH* F: 5′-TGCACCACCAACTGCTTAGC-3′, *GAPDH* R: 5′-GGCATGGACTGTGGTCATGAG-3′.

Statistical analysis

Statistics were performed with Excel (Microsoft). Normality of the data was examined with the Shapiro-Wilk test and a quantile–quantile plot. For data that followed a normal distribution, a variance hypothesis (*F* test of two sample for variances) was tested before the analysis with a Student's two-sample, unpaired *t* test. If data did not follow a normal distribution, a Mann–Whitney test for two independent samples was conducted. For Fig. 9 B, a *z*-value was obtained with a probability-density function, calculated for relative proportions (percentage values) in which the normality of the data was not presumed. In all normalizations to WT expression/protein levels, the mean value obtained from the WT data was set to 1, and the individual intensity data for the WT and knockout cells/lysates were normalized to that value. For quantitative PCR, both WT and individual data points were normalized to GAPDH before further normalization, as explained. Although this method always sets the WT to 1, it allows presentation of the SEM from individual, normalized data points. The Geneious (Biomatters Ltd.) analysis tool was used to construct sequence alignments in Fig. S4 D.

Online supplemental material

Fig. S1 shows an example of cell-to-cell variation in UNC-45a localization to contractile stress fibers and NM-IIA and UNC-45a photoactivation images. Fig. S2 illustrates the mechanism of UNC-45a localization to contractile stress fibers and the effects of its depletion on diphosphorylated (pp)-RLC, NM-IIA, NM-IIB, Hsp90β, and β-actin protein levels in the cells. Fig. S3 shows the RNAi phenotypes after UNC-45a knockout, NM-IIB localization in UNC-45a knockout cells, and analysis of unipolar myosin II structures in WT and UNC-45a knockout U2OS cells. Fig. S4 shows the analysis of different UNC-45a knockout clones and expression of UNC-45a mutant constructs in U2OS cells. Further, it demonstrates six different UNC-45a knockout clones sharing identical phenotypes and being prone to myosin II aggregation. Fig. S5 shows that deletion of the conserved loop in the UNC-45a UCS domain does not compromise NM-IIA folding, whereas the intact UNC-45a domain composition is necessary for actomyosin bundle assembly

and normal 2D migration. Videos 1 and 2 show the random migration of a typical WT and UNC-45a, respectively, knockout cell. Table S1 describes the complete list of biotinylated proteins from the BioID screen by BirA-tagged human UNC-45a in WT U2OS cells.

References

Anderson, M.J., V.N. Pham, A.M. Vogel, B.M. Weinstein, and B.L. Roman. 2008. Loss of unc45a precipitates arteriovenous shunting in the aortic arches. *Dev. Biol.* 318:258–267. https://doi.org/10.1016/j.ydbio.2008.03.022

Baird, M.A., N. Billington, A. Wang, R.S. Adelstein, J.R. Sellers, R.S. Fischer, and C.M. Waterman. 2017. Local pulsatile contractions are an intrinsic property of the myosin 2A motor in the cortical cytoskeleton of adherent cells. *Mol. Biol. Cell.* 28:240–251. https://doi.org/10.1091/mbc.E16-05-0335

Barral, J.M., C.C. Bauer, I. Ortiz, and H.F. Epstein. 1998. Unc-45 mutations in *Caenorhabditis elegans* implicate a CRO1/She4p-like domain in myosin assembly. *J. Cell Biol.* 143:1215–1225. https://doi.org/10.1083/jcb.143.5.1215

Barral, J.M., A.H. Hutagalung, A. Brinker, F.U. Hartl, and H.F. Epstein. 2002. Role of the myosin assembly protein UNC-45 as a molecular chaperone for myosin. *Science.* 295:669–671. https://doi.org/10.1126/science.1066648

Bazzaro, M., A. Santillan, Z. Lin, T. Tang, M.K. Lee, R.E. Bristow, IeM. Shih, and R.B. Roden. 2007. Myosin II co-chaperone general cell UNC-45 overexpression is associated with ovarian cancer, rapid proliferation, and motility. *Am. J. Pathol.* 171:1640–1649. https://doi.org/10.2353/ajpath.2007.070325

Beach, J.R., K.S. Bruun, L. Shao, D. Li, Z. Swider, K. Remmert, Y. Zhang, M.A. Conti, R.S. Adelstein, N.M. Rusan, et al. 2017. Actin dynamics and competition for myosin monomer govern the sequential amplification of myosin filaments. *Nat. Cell Biol.* 19:85–93. https://doi.org/10.1038/ncb3463

Berg, J.S., and R.E. Cheney. 2002. Myosin-X is an unconventional myosin that undergoes intrafilopodial motility. *Nat. Cell Biol.* 4:246–250. https://doi.org/10.1038/ncb762

Berg, J.S., B.C. Powell, and R.E. Cheney. 2001. A millennial myosin census. *Mol. Biol. Cell.* 12:780–794. https://doi.org/10.1091/mbc.12.4.780

Billington, N., A. Wang, J. Mao, R.S. Adelstein, and J.R. Sellers. 2013. Characterization of three full-length human nonmuscle myosin II paralogs. *J. Biol. Chem.* 288:33398–33410. https://doi.org/10.1074/jbc.M113.499848

Bird, J.E., Y. Takagi, N. Billington, M.-P. Strub, J.R. Sellers, and T.B. Friedman. 2014. Chaperone-enhanced purification of unconventional myosin 15, a molecular motor specialized for stereocilia protein trafficking. *Proc. Natl. Acad. Sci. USA.* 111:12390–12395. https://doi.org/10.1073/pnas.1409459111

Blanchoin, L., R. Boujemaa-Paterski, C. Sykes, and J. Plastino. 2014. Actin dynamics, architecture, and mechanics in cell motility. *Physiol. Rev.* 94:235–263. https://doi.org/10.1152/physrev.00018.2013

Breiman, L. 2001. Random forests. *Mach. Learn.* 45:5–32. https://doi.org/10.1023/A:1010933404324

Bujalowski, P.J., P. Nicholls, and A.F. Oberhauser. 2014. UNC-45B chaperone: the role of its domains in the interaction with the myosin motor domain. *Biophys. J.* 107:654–661. https://doi.org/10.1016/j.bpj.2014.05.045

Burgess, S.A., S. Yu, M.L. Walker, R.J. Hawkins, J.M. Chalovich, and P.J. Knight. 2007. Structures of smooth muscle myosin and heavy meromyosin in the folded, shutdown state. *J. Mol. Biol.* 372:1165–1178. https://doi.org/10.1016/j.jmb.2007.07.014

Burnette, D.T., S. Manley, P. Sengupta, R. Sougrat, M.W. Davidson, B. Kachar, and J. Lippincott-Schwartz. 2011. A role for actin arcs in the leading-edge advance of migrating cells. *Nat. Cell Biol.* 13:371–381. https://doi.org/10.1038/ncb2205

Burnette, D.T., L. Shao, C. Ott, A.M. Pasapera, R.S. Fischer, M.A. Baird, C. Der Loughian, H. Delanoe-Ayari, M.J. Paszek, M.W. Davidson, et al. 2014. A contractile and counterbalancing adhesion system controls the 3D shape of crawling cells. *J. Cell Biol.* 205:83–96. https://doi.org/10.1083/jcb.201311104

Case, L.B., M.A. Baird, G. Shtengel, S.L. Campbell, H.F. Hess, M.W. Davidson, and C.M. Waterman. 2015. Molecular mechanism of vinculin activation and nanoscale spatial organization in focal adhesions. *Nat. Cell Biol.* 17:880–892. https://doi.org/10.1038/ncb3180

Chadli, A., J.D. Graham, M.G. Abel, T.A. Jackson, D.F. Gordon, W.M. Wood, S.J. Felts, K.B. Horwitz, and D. Toft. 2006. GCUNC-45 is a novel regulator for the progesterone receptor/hsp90 chaperoning pathway. *Mol. Cell. Biol.* 26:1722–1730. https://doi.org/10.1128/MCB.26.5.1722-1730.2006

Chadli, A., S.J. Felts, and D.O. Toft. 2008. GCUNC45 is the first Hsp90 co-chaperone to show alpha/beta isoform specificity. *J. Biol. Chem.* 283:9509–9512. https://doi.org/10.1074/jbc.C800017200

Chen, D., S. Li, R. Singh, S. Spinette, R. Sedlmeier, and H.F. Epstein. 2012. Dual function of the UNC-45b chaperone with myosin and GATA4 in cardiac development. *J. Cell Sci.* 125:3893–3903. https://doi.org/10.1242/jcs.106435

Choi, C.K., M. Vicente-Manzanares, J. Zareno, L.A. Whitmore, A. Mogilner, and A.R. Horwitz. 2008. Actin and α-actinin orchestrate the assembly and maturation of nascent adhesions in a myosin II motor-independent manner. *Nat. Cell Biol.* 10:1039–1050. https://doi.org/10.1038/ncb1763

Chow, D., R. Srikakulam, Y. Chen, and D.A. Winkelmann. 2002. Folding of the striated muscle myosin motor domain. *J. Biol. Chem.* 277:36799–36807. https://doi.org/10.1074/jbc.M204101200

Clarke, M.S.F., R.W. Caldwell, H. Chiao, K. Miyake, and P.L. McNeil. 1995. Contraction-induced cell wounding and release of fibroblast growth factor in heart. *Circ. Res.* 76:927–934. https://doi.org/10.1161/01.RES.76.6.927

Comyn, S.A., and D. Pilgrim. 2012. Lack of developmental redundancy between Unc45 proteins in zebrafish muscle development. *PLoS One.* 7:e48861. https://doi.org/10.1371/journal.pone.0048861

Craig, R., and J.L. Woodhead. 2006. Structure and function of myosin filaments. *Curr. Opin. Struct. Biol.* 16:204–212. https://doi.org/10.1016/j.sbi.2006.03.006

Epping, M.T., L.A. Meijer, J.L. Bos, and R. Bernards. 2009. UNC45A confers resistance to histone deacetylase inhibitors and retinoic acid. *Mol. Cancer Res.* 7:1861–1870. https://doi.org/10.1158/1541-7786.MCR-09-0187

Epstein, H.F., and J.N. Thomson. 1974. Temperature-sensitive mutation affecting myofilament assembly in *Caenorhabditis elegans*. *Nature.* 250:579–580. https://doi.org/10.1038/250579a0

Etard, C., U. Roostalu, and U. Strähle. 2008. Shuttling of the chaperones Unc45b and Hsp90a between the A band and the Z line of the myofibril. *J. Cell Biol.* 180:1163–1175. https://doi.org/10.1083/jcb.200709128

Etard, C., U. Roostalu, and U. Strähle. 2010. Lack of Apobec2-related proteins causes a dystrophic muscle phenotype in zebrafish embryos. *J. Cell Biol.* 189:527–539. https://doi.org/10.1083/jcb.200912125

Fenix, A.M., N. Taneja, C.A. Buttler, J. Lewis, S.B. Van Engelenburg, R. Ohi, and D.T. Burnette. 2016. Expansion and concatenation of non-muscle myosin IIA filaments drive cellular contractile system formation during interphase and mitosis. *Mol. Biol. Cell.* 27:1465–1478. https://doi.org/10.1091/mbc.E15-10-0725

Gaiser, A.M., C.J.O. Kaiser, V. Haslbeck, and K. Richter. 2011. Downregulation of the Hsp90 system causes defects in muscle cells of Caenorhabditis elegans. *PLoS One.* 6:e25485. https://doi.org/10.1371/journal.pone.0025485

Gazda, L., W. Pokrzywa, D. Hellerschmied, T. Löwe, I. Forné, F. Mueller-Planitz, T. Hoppe, and T. Clausen. 2013. The myosin chaperone UNC-45 is organized in tandem modules to support myofilament formation in C. elegans. *Cell.* 152:183–195. https://doi.org/10.1016/j.cell.2012.12.025

Geach, T.J., and L.B. Zimmerman. 2010. Paralysis and delayed Z-disc formation in the *Xenopus tropicalis* unc45b mutant dicky ticker. *BMC Dev. Biol.* 10:75. https://doi.org/10.1186/1471-213X-10-75

Gibala, M.J., J.D. MacDougall, M.A. Tarnopolsky, W.T. Stauber, and A. Elorriaga. 1995. Changes in human skeletal muscle ultrastructure and force production after acute resistance exercise. *J. Appl. Physiol.* 78:702–708.

Guo, W., D. Chen, Z. Fan, and H.F. Epstein. 2011. Differential turnover of myosin chaperone UNC-45A isoforms increases in metastatic human breast cancer. *J. Mol. Biol.* 412:365–378. https://doi.org/10.1016/j.jmb.2011.07.012

Gustafsson, M.G.L. 2005. Nonlinear structured-illumination microscopy: widefield fluorescence imaging with theoretically unlimited resolution. *Proc. Natl. Acad. Sci. USA.* 102:13081–13086. https://doi.org/10.1073/pnas.0406877102

Henderson, C.J., E. Aleo, A. Fontanini, R. Maestro, G. Paroni, and C. Brancolini. 2005. Caspase activation and apoptosis in response to proteasome inhibitors. *Cell Death Differ.* 12:1240–1254. https://doi.org/10.1038/sj.cdd.4401729

Horvath, P., T. Wild, U. Kutay, and G. Csucs. 2011. Machine learning improves the precision and robustness of high-content screens: using nonlinear multiparametric methods to analyze screening results. *J. Biomol. Screen.* 16:1059–1067. https://doi.org/10.1177/1087057111414878

Hotulainen, P., and P. Lappalainen. 2006. Stress fibers are generated by two distinct actin assembly mechanisms in motile cells. *J. Cell Biol.* 173:383–394. https://doi.org/10.1083/jcb.200511093

Hu, S., K. Dasbiswas, Z. Guo, Y.-H. Tee, V. Thiagarajan, P. Hersen, T.-L. Chew, S.A. Safran, R. Zaidel-Bar, and A.D. Bershadsky. 2017. Long-range self-organization of cytoskeletal myosin II filament stacks. *Nat. Cell Biol.* 19:133–141. https://doi.org/10.1038/ncb3466

Iizuka, Y., F. Cichocki, A. Sieben, F. Sforza, R. Karim, K. Coughlin, R. Isaksson Vogel, R. Gavioli, V. McCullar, T. Lenvik, et al. 2015. UNC-45A Is a Nonmuscle Myosin IIA Chaperone Required for NK Cell Cytotoxicity via Control of Lytic Granule Secretion. *J. Immunol.* 195:4760–4770. https://doi.org/10.4049/jimmunol.1500979

Jorrisch, M.H., W. Shih, and S. Yamada. 2013. Myosin IIA deficient cells migrate efficiently despite reduced traction forces at cell periphery. *Biol. Open.* 2:368–372. https://doi.org/10.1242/bio.20133707

Kamentsky, L., T.R. Jones, A. Fraser, M.-A. Bray, D.J. Logan, K.L. Madden, V. Ljosa, C. Rueden, K.W. Eliceiri, and A.E. Carpenter. 2011. Improved structure, function and compatibility for CellProfiler: modular high-throughput image analysis software. *Bioinformatics.* 27:1179–1180. https://doi.org/10.1093/bioinformatics/btr095

Lam, A.J., F. St-Pierre, Y. Gong, J.D. Marshall, P.J. Cranfill, M.A. Baird, M.R. McKeown, J. Wiedenmann, M.W. Davidson, M.J. Schnitzer, et al. 2012. Improving FRET dynamic range with bright green and red fluorescent proteins. *Nat. Methods.* 9:1005–1012. https://doi.org/10.1038/nmeth.2171

Landsverk, M.L., S. Li, A.H. Hutagalung, A. Najafov, T. Hoppe, J.M. Barral, and H.F. Epstein. 2007. The UNC-45 chaperone mediates sarcomere assembly through myosin degradation in *Caenorhabditis elegans*. *J. Cell Biol.* 177:205–210. https://doi.org/10.1083/jcb.200607084

Lee, D.H., and A.L. Goldberg. 1998. Proteasome inhibitors: valuable new tools for cell biologists. *Trends Cell Biol.* 8:397–403. https://doi.org/10.1016/S0962-8924(98)01346-4

Lee, C.F., G.C. Melkani, Q. Yu, J.A. Suggs, W.A. Kronert, Y. Suzuki, L. Hipolito, M.G. Price, H.F. Epstein, and S.I. Bernstein. 2011. Drosophila UNC-45 accumulates in embryonic blastoderm and in muscles, and is essential for muscle myosin stability. *J. Cell Sci.* 124:699–705. https://doi.org/10.1242/jcs.078964

Lee, C.F., G.C. Melkani, and S.I. Bernstein. 2014. The UNC-45 myosin chaperone: from worms to flies to vertebrates. *Int. Rev. Cell Mol. Biol.* 313:103–144. https://doi.org/10.1016/B978-0-12-800177-6.00004-9

Liu, H., and J.H. Naismith. 2008. An efficient one-step site-directed deletion, insertion, single and multiple-site plasmid mutagenesis protocol. *BMC Biotechnol.* 8:91. https://doi.org/10.1186/1472-6750-8-91

Liu, L., R. Srikakulam, and D.A. Winkelmann. 2008. Unc45 activates Hsp90-dependent folding of the myosin motor domain. *J. Biol. Chem.* 283:13185–13193. https://doi.org/10.1074/jbc.M800757200

McNeil, P.L., and R. Khakee. 1992. Disruptions of muscle fiber plasma membranes. Role in exercise-induced damage. *Am. J. Pathol.* 140:1097–1109.

Mehta, A.D., R.S. Rock, M. Rief, J.A. Spudich, M.S. Mooseker, and R.E. Cheney. 1999. Myosin-V is a processive actin-based motor. *Nature.* 400:590–593. https://doi.org/10.1038/23072

Melkani, G.C., C.F. Lee, A. Cammarato, and S.I. Bernstein. 2010. Drosophila UNC-45 prevents heat-induced aggregation of skeletal muscle myosin and facilitates refolding of citrate synthase. *Biochem. Biophys. Res. Commun.* 396:317–322. https://doi.org/10.1016/j.bbrc.2010.04.090

Melkani, G.C., R. Bodmer, K. Ocorr, and S.I. Bernstein. 2011. The UNC-45 chaperone is critical for establishing myosin-based myofibrillar organization and cardiac contractility in the *Drosophila* heart model. *PLoS One.* 6:e22579. https://doi.org/10.1371/journal.pone.0022579

Myhre, J.L., J.A. Hills, F. Jean, and D.B. Pilgrim. 2014. Unc45b is essential for early myofibrillogenesis and costamere formation in zebrafish. *Dev. Biol.* 390:26–40. https://doi.org/10.1016/j.ydbio.2014.02.022

Nambiar, R., R.E. McConnell, and M.J. Tyska. 2009. Control of cell membrane tension by myosin-I. *Proc. Natl. Acad. Sci. USA.* 106:11972–11977. https://doi.org/10.1073/pnas.0901641106

Ni, W., A.H. Hutagalung, S. Li, and H.F. Epstein. 2011. The myosin-binding UCS domain but not the Hsp90-binding TPR domain of the UNC-45 chaperone is essential for function in *Caenorhabditis elegans*. *J. Cell Sci.* 124:3164–3173. https://doi.org/10.1242/jcs.087320

Niederman, R., and T.D. Pollard. 1975. Human platelet myosin, II: In vitro assembly and structure of myosin filaments. *J. Cell Biol.* 67:72–92. https://doi.org/10.1083/jcb.67.1.72

Odronitz, F., and M. Kollmar. 2007. Drawing the tree of eukaryotic life based on the analysis of 2,269 manually annotated myosins from 328 species. *Genome Biol.* 8:R196. https://doi.org/10.1186/gb-2007-8-9-r196

Paulsen, G., F. Lauritzen, M.L. Bayer, J.M. Kalhovde, I. Ugelstad, S.G. Owe, J. Hallén, L.H. Bergersen, and T. Raastad. 2009. Subcellular movement and expression of HSP27, alphaB-crystallin, and HSP70 after two bouts of eccentric exercise in humans. *J. Appl. Physiol.* 107:570–582. https://doi.org/10.1152/japplphysiol.00209.2009

Price, M.G., M.L. Landsverk, J.M. Barral, and H.F. Epstein. 2002. Two mammalian UNC-45 isoforms are related to distinct cytoskeletal and muscle-specific functions. *J. Cell Sci.* 115:4013–4023. https://doi.org/10.1242/jcs.00108

Ran, F.A., P.D. Hsu, J. Wright, V. Agarwala, D.A. Scott, and F. Zhang. 2013. Genome engineering using the CRISPR-Cas9 system. *Nat. Protoc.* 8:2281–2308. https://doi.org/10.1038/nprot.2013.143

Raucher, D., and M.P. Sheetz. 2000. Cell spreading and lamellipodial extension rate is regulated by membrane tension. *J. Cell Biol.* 148:127–136. https://doi.org/10.1083/jcb.148.1.127

Roux, K.J., D.I. Kim, M. Raida, and B. Burke. 2012. A promiscuous biotin ligase fusion protein identifies proximal and interacting proteins in mammalian cells. *J. Cell Biol.* 196:801–810. https://doi.org/10.1083/jcb.201112098

Sandquist, J.C., and A.R. Means. 2008. The C-terminal tail region of nonmuscle myosin II directs isoform-specific distribution in migrating cells. *Mol. Biol. Cell.* 19:5156–5167. https://doi.org/10.1091/mbc.E08-05-0533

Schneider, C.A., W.S. Rasband, and K.W. Eliceiri. 2012. NIH Image to ImageJ: 25 years of image analysis. *Nat. Methods.* 9:671–675. https://doi.org/10.1038/nmeth.2089

Schulze, N., M. Graessl, A. Blancke Soares, M. Geyer, L. Dehmelt, and P. Nalbant. 2014. FHOD1 regulates stress fiber organization by controlling the dynamics of transverse arcs and dorsal fibers. *J. Cell Sci.* 127:1379–1393. https://doi.org/10.1242/jcs.134627

Shih, W., and S. Yamada. 2010. Myosin IIA dependent retrograde flow drives 3D cell migration. *Biophys. J.* 98:L29–L31. https://doi.org/10.1016/j.bpj.2010.02.028

Shutova, M., C. Yang, J.M. Vasiliev, and T. Svitkina. 2012. Functions of nonmuscle myosin II in assembly of the cellular contractile system. *PLoS One.* 7:e40814. https://doi.org/10.1371/journal.pone.0040814

Shutova, M.S., W.A. Spessott, C.G. Giraudo, and T. Svitkina. 2014. Endogenous species of mammalian nonmuscle myosin IIA and IIB include activated monomers and heteropolymers. *Curr. Biol.* 24:1958–1968. https://doi.org/10.1016/j.cub.2014.07.070

Skau, C.T., R.S. Fischer, P. Gurel, H.R. Thiam, A. Tubbs, M.A. Baird, M.W. Davidson, M. Piel, G.M. Alushin, A. Nussenzweig, et al. 2016. FMN2 Makes Perinuclear Actin to Protect Nuclei during Confined Migration and Promote Metastasis. *Cell.* 167:1571–1585.e18. https://doi.org/10.1016/j.cell.2016.10.023

Srikakulam, R., L. Liu, and D.A. Winkelmann. 2008. Unc45b forms a cytosolic complex with Hsp90 and targets the unfolded myosin motor domain. *PLoS One.* 3:e2137. https://doi.org/10.1371/journal.pone.0002137

Thoresen, T., M. Lenz, and M.L. Gardel. 2013. Thick filament length and isoform composition determine self-organized contractile units in actomyosin bundles. *Biophys. J.* 104:655–665. https://doi.org/10.1016/j.bpj.2012.12.042

Toi, H., K. Fujimura-Kamada, K. Irie, Y. Takai, S. Todo, and K. Tanaka. 2003. She4p/Dim1p interacts with the motor domain of unconventional myosins in the budding yeast, *Saccharomyces cerevisiae. Mol. Biol. Cell.* 14:2237–2249. https://doi.org/10.1091/mbc.E02-09-0616

Tojkander, S., G. Gateva, G. Schevzov, P. Hotulainen, P. Naumanen, C. Martin, P.W. Gunning, and P. Lappalainen. 2011. A molecular pathway for myosin II recruitment to stress fibers. *Curr. Biol.* 21:539–550. https://doi.org/10.1016/j.cub.2011.03.007

Tojkander, S., G. Gateva, and P. Lappalainen. 2012. Actin stress fibers--assembly, dynamics and biological roles. *J. Cell Sci.* 125:1855–1864. https://doi.org/10.1242/jcs.098087

Tojkander, S., G. Gateva, A. Husain, R. Krishnan, and P. Lappalainen. 2015. Generation of contractile actomyosin bundles depends on mechanosensitive actin filament assembly and disassembly. *eLife.* 4:e06126. https://doi.org/10.7554/eLife.06126

Umemoto, S., A.R. Bengur, and J.R. Sellers. 1989. Effect of multiple phosphorylations of smooth muscle and cytoplasmic myosins on movement in an in vitro motility assay. *J. Biol. Chem.* 264:1431–1436.

Venolia, L., W. Ao, S. Kim, C. Kim, and D. Pilgrim. 1999. unc-45 gene of Caenorhabditis elegans encodes a muscle-specific tetratricopeptide repeat-containing protein. *Cell Motil. Cytoskeleton.* 42:163–177. https://doi.org/10.1002/(SICI)1097-0169(1999)42:3<163::AID-CM1>3.0.CO;2-E

Vicente-Manzanares, M., J. Zareno, L. Whitmore, C.K. Choi, and A.F. Horwitz. 2007. Regulation of protrusion, adhesion dynamics, and polarity by myosins IIA and IIB in migrating cells. *J. Cell Biol.* 176:573–580. https://doi.org/10.1083/jcb.200612043

Vicente-Manzanares, M., X. Ma, R.S. Adelstein, and A.R. Horwitz. 2009. Non-muscle myosin II takes centre stage in cell adhesion and migration. *Nat. Rev. Mol. Cell Biol.* 10:778–790. https://doi.org/10.1038/nrm2786

Wei, Q., and R.S. Adelstein. 2000. Conditional expression of a truncated fragment of nonmuscle myosin II-A alters cell shape but not cytokinesis in HeLa cells. *Mol. Biol. Cell.* 11:3617–3627. https://doi.org/10.1091/mbc.11.10.3617

Wells, A.L., A.W. Lin, L.Q. Chen, D. Safer, S.M. Cain, T. Hasson, B.O. Carragher, R.A. Milligan, and H.L. Sweeney. 1999. Myosin VI is an actin-based motor that moves backwards. *Nature.* 401:505–508. https://doi.org/10.1038/46835

Wohlgemuth, S.L., B.D. Crawford, and D.B. Pilgrim. 2007. The myosin co-chaperone UNC-45 is required for skeletal and cardiac muscle function in zebrafish. *Dev. Biol.* 303:483–492. https://doi.org/10.1016/j.ydbio.2006.11.027

Wolfenson, H., A. Bershadsky, Y.I. Henis, and B. Geiger. 2011. Actomyosin-generated tension controls the molecular kinetics of focal adhesions. *J. Cell Sci.* 124:1425–1432. https://doi.org/10.1242/jcs.077388

Ye, J., G. Coulouris, I. Zaretskaya, I. Cutcutache, S. Rozen, and T.L. Madden. 2012. Primer-BLAST: a tool to design target-specific primers for polymerase chain reaction. *BMC Bioinformatics.* 13:134. https://doi.org/10.1186/1471-2105-13-134